

# Photoevaporation of Cosmological Minihalos during Reionization

Paul R. Shapiro<sup>1</sup>, Ilian T. Iliev,<sup>2</sup> and Alejandro C. Raga<sup>3</sup>

<sup>1</sup> *Department of Astronomy, University of Texas, Austin, TX 78712-1083*

<sup>2</sup> *Osservatorio Astrofisico di Arcetri, Largo Enrico Fermi 5, 50125 Firenze, Italy*

<sup>3</sup> *Instituto de Ciencias Nucleares, Universidad Nacional Autonoma de México (UNAM), Apdo. Postal 70-543, 04510 México, D. F., México*

1 November 2018

## ABSTRACT

Energy released by a small fraction of the baryons in the universe, which condensed out while the IGM was cold, dark, and neutral, reheated and reionized it by redshift 6, exposing other baryons already condensed into dwarf-galaxy minihalos to the glare of ionizing radiation. We present the first gas dynamical simulations of the photoevaporation of cosmological minihalos overtaken by the ionization fronts which swept through the IGM during the reionization epoch in the currently-favored  $\Lambda$ CDM universe, including the effects of radiative transfer. These simulations demonstrate the phenomenon of I-front trapping inside minihalos, in which the weak, R-type fronts which traveled supersonically across the IGM decelerated when they encountered the dense, neutral gas inside minihalos, and were thereby transformed into D-type I-fronts, preceded by shock waves. For a minihalo with virial temperature below  $10^4$  K, the I-front gradually burned its way through the minihalo which trapped it, removing all of its baryonic gas by causing a supersonic, evaporative wind to blow backwards into the IGM, away from the exposed layers of minihalo gas just behind the advancing I-front. We describe this process in detail, along with some of its observable consequences, for the illustrative case of a minihalo of total mass  $10^7 M_\odot$ , exposed to a distant source of ionizing radiation with either a stellar or quasar-like spectrum, after it was overtaken at redshift  $z = 9$  by the weak, R-type I-front which ionized the IGM surrounding the source. For a source at  $z = 9$  which emits  $10^{56}$  ionizing photons per second at 1 Mpc (or, equivalently,  $10^{52}$  ionizing photons per second at 10 kpc), the photoevaporation of this minihalo takes about 100–150 Myrs, depending on the source spectrum, ending at about  $z = 7$ – $7.5$ .

Such hitherto neglected feedback effects were widespread during the reionization epoch. N-body simulations and analytical estimates of halo formation in the  $\Lambda$ CDM model suggest that sub-kpc minihalos such as these, with virial temperatures below  $10^4$  K, were so common as to cover the sky around larger-mass source halos and possibly dominate the absorption of ionizing photons during reionization. This means that previous estimates of the number of ionizing photons per H atom required to complete reionization which neglected this effect may be too low. Regardless of their effect on the progress of reionization, however, the minihalos were so abundant that random lines of sight thru the high- $z$  universe should encounter many of them, which suggests that it may be possible to observe the processes described here in the absorption spectra of distant sources.

**Key words:** hydrodynamics—radiative transfer—galaxies: halos—galaxies: high-redshift—intergalactic medium—cosmology: theory

arXiv:astro-ph/0307266v1 13 Jul 2003

## 1 INTRODUCTION

### 1.1 The reionization epoch

Observations of the intergalactic medium (IGM) indicate that the universe was reionized by  $z \approx 6$  but that reionization began much before this. The absence of a Gunn-Peterson (GP) trough in the spectra of high-redshift quasars at observed wavelengths  $\lambda_\alpha(1+z)$  due to Ly $\alpha$  resonance scattering by H atoms in the IGM at  $z < 6$  indicates that the IGM was very highly ionized at all  $z < 6$  (Fan et al. 2000). Since the universe recombined at  $z \sim 1000$ , something must have occurred to reionize it by  $z \sim 6$ .

The detection of GP troughs in the spectra of SDSS quasars at  $z \geq 6$  places a lower limit on the mean H I density in the IGM at  $z = 6$  large enough to suggest that reionization might only just have ended at  $z \approx 6$  (Becker et al. 2001; Djorgovski et al. 2001; Fan et al. 2003). Limits on the GP effect at  $z < 6$ , that is, imply a hydrogen neutral fraction significantly *smaller* than the value at  $z = 6$ , which can be explained by a photoionized IGM only if the ionizing background radiation increased dramatically in a short interval of cosmic time at this epoch (Fan et al. 2002; Cen & McDonald 2002). Since reionization is believed to have proceeded inhomogeneously, with isolated patches of ionized gas which eventually grew to fill all of space, the epoch of overlap would have been accompanied by the required rapid increase in the ionizing radiation background, as the absorption mean free path for this radiation suddenly increased. For this reason, the GP detections at  $z = 6$  and limits at  $z < 6$  are thought to indicate that the epoch of overlap – the end of reionization – occurred at a redshift close to  $z = 6$ .

The recent discovery by the WMAP satellite of polarization of the CMB which fluctuates on an angular scale of  $10^\circ$ , on the other hand, amounts to a detection of a foreground electron scattering optical depth through the IGM of  $\tau_{es} \simeq 0.17 \pm 0.04$  (Kogut et al. 2003; Spergel et al. 2003). This suggests that the IGM was either mostly ionized by a redshift of  $z \simeq 17 \pm 5$ , or else was at least partially ionized starting at even higher  $z$  (Spergel et al. 2003). The GP detection at  $z = 6$  described above argues against the simplest interpretation of the WMAP polarization result in which the universe was fully reionized by redshift  $z \gtrsim 15$  and stayed ionized thereafter. Another argument against that simple interpretation is based upon the fact that, after the IGM was reheated by its reionization, it would gradually have cooled by adiabatic expansion even though it continued to be photoionized by background radiation. If reionization finished as early as implied by the simplest interpretation of the WMAP results, this would have lowered the temperature of the IGM at redshifts  $z \leq 4$  below the level deduced from the Ly  $\alpha$  forest (Hui & Haiman 2003).

In short, reionization is currently believed to have begun by redshift  $z \gtrsim 15$  to accommodate the WMAP results but to extend until  $z = 6$  to accommodate observations of the GP effect and of the Ly  $\alpha$  forest at  $z \leq 6$ . When and how this reionization occurred and what its consequences were for the

subsequent epochs is one of the major unsolved problems of cosmology.

### 1.2 Ionization fronts in the IGM

The neutral, opaque IGM out of which the first bound objects condensed was dramatically reheated and reionized at some time between a redshift  $z \approx 30$  and  $z \approx 6$  by the radiation released by some of these objects. When the first sources turned on, they ionized their surroundings by propagating weak, R-type ionization fronts which moved outward supersonically with respect to both the neutral gas ahead of and the ionized gas behind the front, racing ahead of the hydrodynamical response of the IGM, as first described by Shapiro (1986) and Shapiro & Giroux (1987). These authors solved the problem of the time-varying radius of a spherical I-front which surrounds an isolated source in a cosmologically-expanding IGM analytically, generalizing the I-front jump condition and radiative transfer to cosmological conditions. They applied these solutions to determine when and how fast the I-fronts surrounding isolated sources would grow to overlap and, thereby, complete the reionization of the universe<sup>1</sup>. The effect of density inhomogeneity on the rate of the I-front propagation was described by a mean “clumping factor”  $C \equiv \langle n^2 \rangle / \langle n \rangle^2 > 1$ , which slowed the I-fronts by increasing the average recombination rate per atom inside clumps. This suffices to describe the rate of I-front propagation as long as the clumps are either not self-shielding or, if so, only absorb a small fraction of the ionizing photons emitted by the central source.

Numerical radiative transfer methods are currently under development to solve this problem in 3-D for the inhomogeneous density distribution which arises as cosmic structure forms, so far primarily limited to the transfer of ionizing radiation through pre-computed density fields generated by cosmological simulations which do not include radiative transfer, so there is no back-reaction of the radiative transfer calculation on the density field or any aspect of the gas dynamics (Razoumov & Scott 1999; Abel, Norman & Madau 1999; Ciardi et al. 2001; Nakamoto, Umemura & Susa 2001; Sokasian et al. 2001; Cen 2002; Hayes & Norman 2002; Ciardi et al. 2003). Approximate approaches which incorporate some of the important effects of radiative transport during reionization within the context of cosmological gas dynamics simulation have also been developed (Gnedin 2000; Gnedin & Abel 2001; Ricotti, Gnedin & Shull 2002a). These recent attempts to model inhomogeneous reionization numerically are generally handicapped by their limited spatial resolution, which prevents them from fully resolving the most important (sub-kpc-sized) density inhomogeneities. The questions of what dynamical effect the I-front

<sup>1</sup> This provided the first indication that quasars alone did not reionize the universe; the observed quasar luminosity function extrapolated to higher redshift was not sufficient to do so in time to satisfy the GP constraint, suggesting that some other source was responsible, such as starlight.

had on the density inhomogeneities it encountered and how the presence of these inhomogeneities affected the I-fronts and reionization, therefore, require further analysis.

Towards this end, we have developed a radiation-hydrodynamics code which incorporates radiative transfer and focused our attention on properly resolving this small-scale structure. Here we shall present in some detail our results of the first radiation-hydrodynamical simulations of the back-reaction of a cosmological I-front on a gravitationally-bound density inhomogeneity it encounters – a  $10^7 M_\odot$  dwarf galaxy minihalo – during reionization, along with some general considerations which apply to other halos as well. A second paper to follow will present the results for a much wider range of cases, with different halo masses and I-front encounter epochs, to quantify just how the process described here varies with these properties. As it turns out, the photoevaporation of sub-kpc-sized objects like these may be the dominant process by which ionizing photons are absorbed during reionization, so this problem is of critical importance. In addition, observations of the absorption spectra of high redshift sources like those which reionized the universe should reveal the presence of these photoevaporative flows and provide a useful diagnostic of the reionization process.

### 1.3 The photoevaporation of dwarf galaxy minihaloes overtaken by cosmological ionization fronts

The effect which small-scale clumpiness had on reionization depended upon the sizes, densities, and spatial distribution of the clumps overtaken by the I-fronts during reionization. For the currently-favored  $\Lambda$ CDM model ( $\Omega_0 = 1 - \lambda_0 = 0.3$ ,  $h = 0.7$ ,  $\Omega_b h^2 = 0.02$ , primordial power spectrum index  $n_p = 1$ ; COBE-normalized), which is the model we adopt throughout this paper, the universe at  $z > 6$  was already filled with dwarf galaxies capable of trapping a piece of the global, intergalactic I-fronts which reionized the universe and photoevaporating their gaseous baryons back into the IGM. Prior to their encounter with these I-fronts, “minihalos” with  $T_{\text{vir}} \leq 10^4 \text{K}$  were neutral and optically thick to hydrogen ionizing radiation, as long as their total mass exceeded the Jeans mass  $M_J$  in the unperturbed background IGM prior to reionization (see § 2), as was required to enable baryons to collapse into the halo along with dark matter. Their “Strömgren numbers”  $L_S \equiv 2R_{\text{halo}}/\ell_S$ , the ratio of a halo’s diameter to its Strömgren length  $\ell_S$  inside the halo (the length of a column of gas within which the unshielded arrival rate of ionizing photons just balances the total recombination rate), were large. For a uniform gas of H density  $n_H$ , located a distance  $r_{\text{Mpc}}$  (in Mpc) from a UV source emitting  $N_{\text{ph},56}$  ionizing photons (in units of  $10^{56} \text{s}^{-1}$ ), the Strömgren length is only  $\ell_S \approx (100 \text{pc})(N_{\text{ph},56}/r_{\text{Mpc}}^2)(n_H/0.1 \text{cm}^{-3})^{-2}$ , so  $L_S \gg 1$  for most of the range of halo masses and sources of interest, as we will discuss in § 2.3. In that case, the intergalactic, weak, R-type I-front which entered each minihalo during reionization would have decelerated to about twice

the sound speed of the ionized gas before it could exit the other side, thereby transforming itself into a D-type front, preceded by a shock. Typically, the side facing the source would then have expelled a supersonic wind backwards toward the source, which shocked the surrounding IGM as the minihalo photoevaporated.

The importance of this photoevaporation process has long been recognized in the study of interstellar clouds exposed to ionizing starlight (Oort & Spitzer 1955; Spitzer 1978; Bertoldi 1989; Bertoldi & McKee 1990; Lefloch & Lazareff 1994; Bertoldi & Draine 1995; Lizano et al. 1996; Gorti & Hollenbach 2001). Radiation-hydrodynamical simulations were performed in 2-D of a stellar I-front overtaking a clump inside a molecular cloud (Klein, Sandford & Whitaker 1982; Sandford, Whitaker & Klein 1983). More recently, 2-D simulations for the case of a circumstellar cloud ionized by a single nearby star have also been performed (Mellema et al. 1998). In the cosmological context, however, the importance of this process has only recently been fully appreciated.

In proposing the expanding minihalo model to explain Lyman  $\alpha$  forest (“LF”) quasar absorption lines, Bond, Szalay & Silk (1988) discussed how gas originally confined by the gravity of dark minihalos in the CDM model with virial temperatures below  $10^4 \text{K}$  would have been expelled by pressure forces if photoionization by ionizing background radiation suddenly heated all the gas to an isothermal condition at  $T \approx 10^4 \text{K}$ , a correct description only in the optically-thin limit. The first realistic discussion of the photoevaporation of such minihaloes by cosmological I-fronts, including the first radiation-hydrodynamical simulations of this process, was by Shapiro, Raga & Mellema (1997, 1998). This work demonstrated the importance of taking proper account of optical depth and self-shielding simultaneously with hydrodynamics, in order to derive the correct dynamical flow, ionization structure and the resulting observational characteristics. Barkana & Loeb (1999) subsequently confirmed the relative importance of this process as a feedback effect on dwarf galaxy minihaloes during reionization, using static models of uniformly-illuminated spherical clouds in thermal and ionization equilibrium, without accounting for gas dynamics. They took H atom self-shielding into account and assumed that all gas which is instantaneously heated above the minihalo virial temperature must be evaporated. They concluded that 50%-90% of the gas in gravitationally-bound objects when reionization occurred should have been evaporated. However, by neglecting the time-dependent gas dynamical nature of this phenomenon, their model failed to capture some essential physics, leading to incorrect results, as we will show below.

Further results of radiation-hydrodynamical simulations of a cosmological minihalo overrun by a weak, R-type I-front in the surrounding IGM were summarized in Shapiro & Raga (2000a,b, 2001) and Shapiro (2001). These results were preliminary versions of the final, more advanced results which we shall present in this paper in some detail. Before we do, it is worth summarizing why we believe that

the particular problem simulated here is not only generic to the minihalos which formed prior to the end of the reionization epoch, but likely to have affected the global outcome of cosmic reionization, as well.

According to the currently prevalent paradigm of cosmic structure formation – the flat, cold-dark matter universe with cosmological constant ( $\Lambda$ CDM) – cosmological structures formed hierarchically, with small mass haloes forming first and merging over time to form ever larger halos. The first baryonic structures to emerge in this way were the “minihalos” which began forming at  $z > 20 - 30$ , with masses in the range from about  $10^4 M_\odot$  to  $10^8 M_\odot$ , where the minimum is set by the Jeans mass in the cold and neutral IGM prior to its reionization. The term “minihalo” used here specifically refers to halos at any epoch with virial temperatures  $T_{\text{vir}} \leq 10^4$  K. In such halos, the thermal collisional ionization rate alone was not sufficient to ionize the H and He atoms significantly, so the minihalo gas was almost entirely neutral, in the absence of ionizing radiation. Moreover, collisional line excitation of H atoms is exponentially suppressed below  $10^4$  K and, thus, a purely atomic gas of H and He could not radiatively cool effectively below that temperature. Such minihalo gas was able to cool below  $10^4$  K only if  $\text{H}_2$  molecules formed in sufficient abundance to cool it by rotational-vibrational line excitation, to temperatures as low as  $T \lesssim 100$  K. This  $\text{H}_2$  formation, catalyzed by the tiny residual ionized fraction, was essential if the minihalo gas was to cool and, thereby, compress relative to the dark matter, enough to become self-gravitating and form stars. Simulations suggest that minihalos of mass  $M \gtrsim 10^6 M_\odot$  did just that, thereby forming the first metal-free (“Pop. III”) stars of mass  $M_* \gtrsim 100 M_\odot$  at  $z \lesssim 30$  (Bromm, Coppi & Larson 2002; Abel, Bryan & Norman 2002), perhaps leading to the first miniquasars, as well.

While this process of star formation in minihalos is important as the origin of the first sources of ionizing radiation in the universe, minihalos are not likely to have been the dominant source of cosmic reionization. The  $\text{H}_2$  formation required for minihalos to form stars would have been suppressed easily by photodissociation in the Lyman-Werner bands by the background of UV radiation created by the very first minihalos which formed stars, when the ionizing radiation background was still much too low to cause reionization (Haiman, Abel & Rees 2000). If so, most minihalos must not have formed stars and must, instead, have remained “sterile”, dark-matter-dominated halos filled with stable, neutral atomic gas at the halo virial temperature  $T_{\text{vir}} \leq 10^4$  K. In that case, when some other source of radiation ionized the universe and drove an I-front into the minihalo, which photoheated the gas to  $T > 10^4$  K, minihalo gravity would have been unable to confine the ionized gas and, eventually, all of it was expelled. A caveat to this description above of the negative feedback on the  $\text{H}_2$  in minihalos due to the first UV sources is the possibility that the presence of a weak X-ray background might have counterbalanced this  $\text{H}_2$  photodissociation by enhancing the  $\text{H}_2$  formation rate in places where X-ray ioniza-

tion increased the small ionized fraction inside the halos (Haiman, Abel & Rees 2000).<sup>2</sup> Apart from such caveats, however, the primary source of reionizing photons is believed to have been the halos with  $T_{\text{vir}} \geq 10^4$  K. For such halos, radiative cooling by H atom line excitation alone was efficient enough to compress the gas to enable self-gravity and self-shielding, leading to star formation. For the purposes of this paper, we shall henceforth accept the premise that the minihalos were predominantly “sterile” targets of source halos with  $T_{\text{vir}} \geq 10^4$  K, of higher mass.

In that case, it has been shown, source halos would generally have found their skies covered by the minihalos between them and neighboring source halos, until the ionization fronts created by those sources overtook the minihalos and photoevaporated them, possibly consuming a significant fraction of the ionizing photons released by the sources in the process (Haiman, Abel & Madau 2001, Shapiro 2001, Barkana & Loeb 2002 and Shapiro et al. 2003). According to these authors, the phenomenon of minihalo photoevaporation during reionization identified by Shapiro, Raga & Mellema (1997, 1998) not only was quite common and had an important negative feedback effect on the minihalos, it also had an important effect on reionization, itself, by screening the ionizing sources and increasing the number of ionizing photons required per baryon to complete reionization. While these results demonstrate the importance of minihalos to the cosmic reionization story, we will show that a correct quantitative estimate of these effects requires detailed gas dynamics and radiative transfer simulations. In addition, as pointed out by Shapiro (2001), there is a very large number of minihalos per unit redshift along an arbitrary line-of-sight (LOS) through the universe at  $z \geq 6$ , so the process of their photoevaporation is potentially observable in the absorption spectra of very high- $z$  sources.

This paper is organized as follows. In § 2, we discuss our minihalo model and the statistics of minihalos in the  $\Lambda$ CDM universe, as well as the analytical expectations for how the photoevaporation of cosmological minihalos proceeds and what its outcome is. In § 3, we outline the basic equations used to model the gas dynamics of photoevaporation, the microphysical processes considered and the initial conditions for our simulations. In § 4, we discuss our numerical method and tests, and the parameters of our simulations. In § 5, we describe the photoevaporation process in detail for the illustrative case of a minihalo of  $10^7 M_\odot$  at  $z = 9$  exposed

<sup>2</sup> The net effect of these early X-rays on the  $\text{H}_2$  in minihalos may have been more negative than positive, however, if they raised the entropy floor of the IGM from which the minihalos condensed (Oh & Haiman 2003). Another study suggests that the near environment of early-star forming halos might also have experienced some *positive* feedback on the  $\text{H}_2$ , which partially offset the negative feedback due to  $\text{H}_2$  dissociation by UV sources, although not necessarily *inside* the pre-existing minihalos (e.g. Ricotti, Gnedin & Shull 2002b); this study did not include an X-ray background.

to ionizing radiation from one of three types of sources: (1) starlight with a 50,000 K black-body spectrum (hereafter, referred to as “BB 5e4”), representative of massive Pop. II stars, (2) starlight with a  $10^5$  K black-body spectrum (hereafter, “BB 1e5”), as expected for massive Pop. III stars, and (3) QSO-like, with a power-law spectrum  $F_\nu \propto \nu^{-1.8}$  ( $\nu > \nu_H$ ) (hereafter, “QSO”). We show our results for the structure of the global I-front propagating in the IGM during its weak, R-type phase (§ 5.1), the encounter between this global I-front and a minihalo along its path and the penetration of the minihalo by the front in its weak, R-type phase (§ 5.2), the trapping of the I-front inside the minihalo and its transition to D-type (§ 5.3), the structure of the photoevaporative flow during the D-type phase (§ 5.4), the evolution of temperature structure (§ 5.5) and I-front location and speed (§ 5.6), the evaporation times (§ 5.7), the consumption of ionizing photons (§ 5.8), and some observational diagnostics (§ 5.9). Finally, in § 6, we give our summary and conclusions.

## 2 ANALYTICAL CONSIDERATIONS

### 2.1 Cosmological minihalos during reionization in a $\Lambda$ CDM Universe

#### 2.1.1 Minihalo model

Our initial minihalo model consists of a virialized region in hydrostatic equilibrium embedded in an exterior region of cosmological infall. For the former, we have previously developed an analytical model for the postcollapse equilibrium structure of virialized objects that condense out of a cosmological background universe, either matter-dominated or flat with a cosmological constant (Shapiro, Iliev & Raga 1999; Iliev & Shapiro 2001). This Truncated Isothermal Sphere, or TIS, model assumes that cosmological halos form from the collapse and virialization of “top-hat” density perturbations and are spherical, isotropic, and isothermal. This leads to a unique, nonsingular TIS, a particular solution of the Lane-Emden equation (suitably modified when  $\Lambda \neq 0$ ). The size  $r_t$  and velocity dispersion  $\sigma_V$  are unique functions of the mass  $M$  and formation redshift  $z_{\text{coll}}$  of the object for a given background universe. The TIS profile flattens to a constant central value,  $\rho_0$ , which is roughly proportional to the critical density of the universe at the epoch of collapse,  $\rho_c(z_{\text{coll}})$ , with a small core radius  $r_0 \approx r_t/30$  [where  $\sigma_V^2 = 4\pi G \rho_0 r_0^2$  and  $r_0 \equiv r_{\text{King}}/3$  for the “King radius”  $r_{\text{King}}$ , defined by Binney & Tremaine (1987), p. 228]. While the TIS model does not produce the central cusp at very small radii in the dark matter density profile of halos predicted by numerical CDM N-body simulations, it does reproduce many of the average properties of these halos remarkably well, suggesting that it is a useful approximation for halos which result from more realistic initial conditions (Shapiro, Iliev & Raga 1999; Iliev & Shapiro 2001, 2002). In particular, the TIS mass profile agrees well with the fit by NFW to numerical simulations (i.e. fractional deviation  $\lesssim 20\%$ ) at all radii outside of a few

TIS core radii (i.e. outside a King radius or so). Our application here of the TIS model is not sensitive to the small difference between the TIS and NFW dark-matter density profiles at small radii. In both cases, the baryonic profile is nonsingular.

The TIS halo is uniquely specified by the central density  $\rho_0$  and core radius  $r_0$ . Since the central density is proportional to  $\rho_c(z_{\text{coll}})$ , it is also possible to specify the profile by the two parameters, total mass and collapse redshift,  $(M, z_{\text{coll}})$ , which is equivalent to specifying the pair  $(r_0, \rho_0)$ . This makes the TIS model extremely useful in combination with other analytical methods which determine the typical epochs of collapse for halos of different masses, such as the well-known Press-Schechter approximation. We note that it is customary elsewhere to define the total mass of profiles used to model CDM halos as  $M_{200}$ , the mass inside a sphere of radius  $r_{200}$  with a mean density which is  $200\rho_c(z)$  at some redshift  $z$ . For the sake of comparison with the TIS profile, if we were to fix  $M_{200}$  and  $r_{200}$  for halos of different profiles, which amounts to fixing  $M$  and  $z_{\text{coll}}$  for the TIS halo, then  $M = 1.167M_{200} = 772.6\rho_0 r_0^3$ ,  $\rho_0 = 18,000\rho_c(z_{\text{coll}})$  and  $r_{200} = 24.2r_0$  if  $z = z_{\text{coll}}$ .

As applied here to model minihalos, the TIS is embedded in a self-similar, spherical, cosmological infall, using the solution for the latter in an Einstein-de Sitter universe derived by Bertschinger (1985), generalized by us to apply it to a low-density background universe at the early times considered here (Iliev & Shapiro 2001, Appendix A). As discussed in detail in Shapiro, Iliev & Raga (1999) and Iliev & Shapiro (2001), the truncation radius of the TIS solution coincides almost exactly with the location of the shock in the self-similar infall solution, allowing a natural match of the two models. The procedure which we used to accomplish that is discussed in detail in the Appendix.

For the calculations in this paper, our fiducial case is a minihalo of mass  $M = 10^7 M_\odot$  which collapses at  $z = 9$ . According to the TIS model, this minihalo has a virial radius  $r_t = 0.76$  kpc, a virial temperature  $T_{\text{vir}} = 4000$  K, and a DM velocity dispersion  $\sigma_V = 5.2 \text{ km s}^{-1}$ . In units of these fiducial values, we define  $M_7 \equiv M/(10^7 M_\odot)$  and  $(1+z)_{10} \equiv (1+z)/10$ . We shall express temperature in terms of  $T_4 = T/(10^4 \text{ K})$ .

#### 2.1.2 Statistical properties of minihalos

This TIS model for the internal structure of an individual minihalo of a given mass  $M$  which forms at a given collapse epoch  $z_{\text{coll}}$  can be combined with the Press-Schechter (PS) approximation to determine the statistical expectations for the properties of halos of different masses at each epoch which result from the Gaussian-random initial fluctuations of the  $\Lambda$ CDM universe.

In Figure 1, we plot the curves in the halo  $M-z_{\text{coll}}$  plane which correspond to halos which collapse from  $\nu$ - $\sigma$  fluctuations for  $\nu = 1, 2$ , and 3. Here  $\nu \equiv \delta_{\text{crit}}/\sigma(M)$ ,  $\sigma(M)$  is the rms fluctuation in the dark matter density field, filtered on mass scale  $M$ , as predicted by linear theory, and  $\delta_{\text{crit}}$  is the

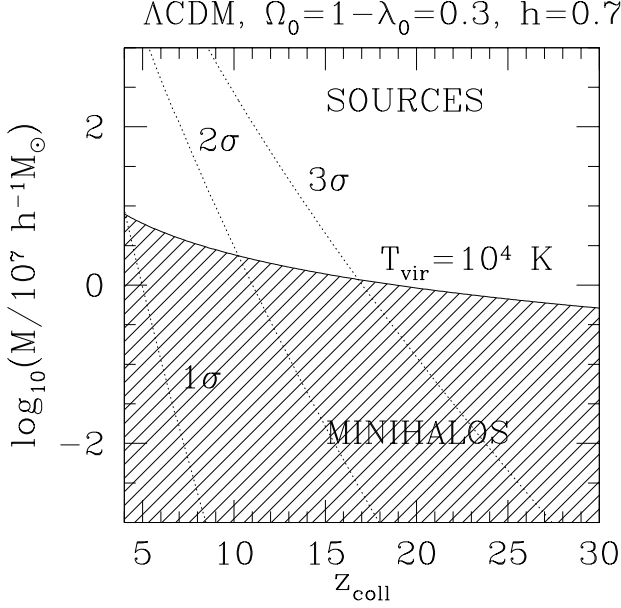


**Figure 1.** How common are minihalos at high redshift? Plot of minihalo mass vs. redshift. Shaded region represents minihalos: halos with virial temperature  $T_{\text{vir}} < 10^4$  K. Dotted curves represent  $\nu - \sigma$  fluctuations with  $\nu = 1, 2$  and  $3$ , predicted by the PS approximation, as labeled.

overdensity of a top-hat perturbation given by extrapolating the linear solution to the time of infinite collapse in the exact nonlinear solution. The value  $\nu = 1$  corresponds to the most common halos, while high values of  $\nu$  correspond to rare density peaks.

The minihalos span a mass range from  $M_{\text{min}}$  to  $M_{\text{max}}$  which varies with redshift, with  $M_{\text{min}}$  close to the Jeans mass of the uncollapsed IGM prior to reionization,

$$M_J = 5.7 \times 10^3 M_\odot \left( \frac{\Omega_0 h^2}{0.15} \right)^{-1/2} \left( \frac{\Omega_b h^2}{0.02} \right)^{-3/5} \times (1+z)_{10}^{3/2}, \quad (1)$$

while

$$M_{\text{max}} = 3.95 \times 10^7 M_\odot \left( \frac{\Omega_0 h^2}{0.15} \right)^{-1/2} (1+z)_{10}^{-3/2} \quad (2)$$

is the mass for which  $T_{\text{vir}} = 10^4$  K according to the TIS model (Iliev & Shapiro 2001). This maximum minihalo mass at each epoch (i.e. the curve of constant  $T_{\text{vir}} = 10^4$  K) is shown in Figure 1. Figure 1 demonstrates that, below redshift  $z \sim 10$ , all minihalos result from fluctuations with  $\nu < 2$ , so they are quite typical and fairly common. Integrating over the entire mass function of minihalos from  $M_{\text{min}}$  to  $M_{\text{max}}$ , we find that the total collapsed mass fraction in minihalos is (36%, 28%, 10%, 3%) at  $z = (6, 9, 15, 20)$ , respectively.

## 2.2 Ionizing flux

We shall assume that each minihalo is photoevaporated by an isotropic point source located at a proper distance  $r$  from the minihalo centre, which emits  $N_{\text{ph}}$  H ionizing photons per second with luminosity  $L_\nu$  ( $\text{erg s}^{-1} \text{Hz}^{-1}$ ), so that

$$N_{\text{ph}} = \int_{\nu_H}^{\infty} d\nu \frac{L_\nu}{h\nu}. \quad (3)$$

The unattenuated flux at the location of the minihalo centre is just  $F_\nu = L_\nu / (4\pi r^2)$ , since  $r \ll c/H(z)$ , the horizon size during minihalo photoevaporation. We shall, henceforth, parametrize the flux to which a given halo is exposed in terms of the dimensionless frequency-integrated photon flux,  $F_0 \equiv N_{\text{ph},56} / r_{\text{Mpc}}^2$ . For example, a source which emits  $10^{56}$  (or  $10^{52}$ ) ionizing photons per second at a distance of 1 Mpc (or 10 kpc) corresponds to  $F_0 = 1$ , or, in physical units, a flux of  $8.356 \times 10^5 \text{ cm}^{-2} \text{ s}^{-1}$ . What values of  $F_0$  are relevant to the encounter between a minihalo and an I-front during cosmic reionization?

To get a sense of how large this fiducial flux is in terms of an equivalent isotropic radiation background, we can estimate the mean ionizing photon intensity  $J_\gamma$  ( $\text{cm}^{-2} \text{ s}^{-1} \text{ster}^{-1}$ ) required to irradiate an atom on the minihalo surface with the same flux, by equating this flux to  $2\pi J_\gamma$ . For a QSO-like ionizing background with a power-law energy spectrum,  $J_\nu \propto \nu^{-\alpha}$ ,  $\alpha > 1$ , for example, the integrated photon intensity is  $J_\gamma = 1.509 \times 10^5 J_{-21} (1 + \alpha)^{-1}$ , where  $J_{-21}$  is the mean intensity at the H Lyman limit in units of  $10^{-21} \text{ erg cm}^{-2} \text{ s}^{-1} \text{Hz}^{-1} \text{ster}^{-1}$ . The equivalent dimensionless flux parameter is then given by

$$F_{0,\text{equ}} = 1.13(1 + \alpha)^{-1} J_{-21}, \quad (4)$$

so  $F_0 = 1$  is roughly equivalent to  $J_{-21} \sim 1$ .

We can estimate the appropriate range to consider for  $F_0$  as follows. Suppose the luminosity of a dwarf galaxy is produced by a super-massive star cluster (SSC). Tan & McKee (2001) estimate the ionizing luminosity of such an SSC, using the observed stellar mass function in the R136 cluster in 30 Doradus as input to the STARBURST99 code of Leitherer et al. (1999), finding (for  $0.1 \leq M_*/M_\odot \leq 100$ ):

$$N_{\text{ph},52} = 3.94 M_{*,6}, \quad (5)$$

where  $M_*$  is the total mass in stars,  $M_p \equiv M / (10^p M_\odot)$  and  $N_{\text{ph},q} \equiv N_{\text{ph}} / (10^q \text{ s}^{-1})$  is the flux of ionizing photons.

Alternatively, Madau & Rees (2000) have estimated that, for a standard Salpeter IMF, approximately 3000 – 4000 ionizing photons are emitted for every stellar baryon. Hence, if the galaxy gas mass turned into stars is  $M_*$ , the total number of ionizing photons emitted during the lifetime of those stars is

$$N_{\text{tot}} = \int N_{\text{ph}} dt \approx 10^{66.6} M_{*,6}. \quad (6)$$

Assuming an average lifetime of  $\tau_{\text{lifetime}} \approx 10^7$  yrs, we obtain

$$N_{\text{ph},52} \approx 1.6 M_{*,6}, \quad (7)$$

similar to the result in equation (5). On the other hand, Bromm, Kudritzki & Loeb (2001) estimate that the number of photons produced per baryon by Pop. III stars can be about 10-20 times higher than this.

If we let  $f_b = \Omega_b/\Omega_0 = 0.136$  be the cosmic mean baryonic mass fraction and  $f_*$  be the fraction of these baryons which are converted into stars in the dwarf galaxy halo, then  $M_* = f_* f_b M_{\text{halo}}$ . Tan & McKee (2001) find  $f_* = 0.5$  for their SSC. If the target minihalo mass  $M_{\text{target}} \ll M_{\text{halo}}$ , the mean distance between source and halo is  $r \approx d_{\text{sep}}/2$ , while if  $M_{\text{target}} \approx M_{\text{halo}}$ , it is  $r = d_{\text{sep}}$ . For source halos of mass  $10^8 M_\odot$  at  $z = 9$ ,  $d_{\text{sep}} \approx 50$  kpc (Shapiro 2001), so  $r_{\text{Mpc}} = (0.5 - 1) \times d_{\text{sep, Mpc}} \approx 0.025 - 0.05$ . The characteristic dimensionless flux  $F_0$  for such sources at this epoch is, therefore, given by

$$F_0 = \frac{N_{\text{ph},56}}{r_{\text{Mpc}}^2} = (1 - 4) \times 3.94 \times 10^{-2} \frac{f_* f_b M_{\text{halo},8}}{d_{\text{sep,Mpc}}^2} \approx 1 - 4, \quad (8)$$

if we adopt the luminosity per gas mass estimated by Tan & McKee (2001). For halos in the dwarf galaxy mass range, the PS approximation for the halo mass function in  $\Lambda$ CDM yields  $dn_{\text{halo}}/dM \propto M^{-2}$  (Shapiro 2001), so the mean separation of dwarf galaxy sources of mass  $M$  is  $d_{\text{sep}} = (M dn_{\text{halo}}/dM)^{-1/3} \propto M^{1/3}$ . If the mass-to-light ratio  $M/L$  is independent of halo mass, then the flux incident on a minihalo due to one of these halos scales only weakly with source halo mass,  $F_0 \propto M^{1/3}$ , up to the galaxy mass scale above which the PS mass function cuts off exponentially, at which point  $F_0$  drops more rapidly with increasing mass.

Finally, we can get a simple, direct estimate of  $F_0$  based on the mean flux required to reionize the universe, as follows. Suppose the universe was filled with sources that supplied  $\bar{\xi}$  ionizing photons per H atom steadily over the time between the source turn-on epoch  $z_{\text{on}}$  and the epoch of reionization overlap at  $z_{\text{ov}}$ . Assuming that all photons remained energetic enough to ionize H atoms despite their continuous redshifting, and neglecting the absorption of these photons during the extended reionization epoch, the mean comoving number density of ionizing photons at any redshift in the range  $z_{\text{on}} \leq z \leq z_{\text{ov}}$  would be just

$$\bar{n}_\gamma = \bar{\xi} \bar{n}_H \frac{t(z) - t_{\text{on}}}{t_{\text{ov}} - t_{\text{on}}}, \quad (9)$$

where  $t$  is the age of the universe at each redshift, as labelled, and  $\bar{n}_H$  here refers to the mean IGM H density. The mean photon intensity  $J_\gamma$  of this isotropic background of ionizing radiation would then be given by

$$J_\gamma = \frac{c}{4\pi} \bar{n}_\gamma = \frac{\bar{\xi} \bar{n}_H c}{4\pi} \frac{t(z) - t_{\text{on}}}{t_{\text{ov}} - t_{\text{on}}} \quad (10)$$

This corresponds to an effective photon flux  $F_{\text{eff}}$  given by

$$F_{\text{eff}} = 2\pi J_\gamma = \frac{\bar{\xi} \bar{n}_H c}{2} \frac{t(z) - t_{\text{on}}}{t_{\text{ov}} - t_{\text{on}}}, \quad (11)$$

or a dimensionless flux

$$F_{0,\text{eff}} = 3\bar{\xi}(1+z)_{10}^3 \left( \frac{\Omega_b h^2}{0.02} \right) \left[ \frac{t(z) - t_{\text{on}}}{t_{\text{ov}} - t_{\text{on}}} \right], \quad (12)$$

For  $t_{\text{on}} \ll t_{\text{ov}}$  the quantity in square brackets can be replaced by  $t(z)/t_{\text{ov}}$  to yield an upper limit,

$$F_{0,\text{eff}} \lesssim 3\bar{\xi}(1+z)_{10}^3 \left( \frac{\Omega_b h^2}{0.02} \right) \left( \frac{1+z}{1+z_{\text{ov}}} \right)^{-3/2}, \quad (13)$$

or, if  $z_{\text{ov}} = 6$  and  $\Omega_b h^2 = 0.02$ ,

$$F_{0,\text{eff}} \lesssim 1.8\bar{\xi}(1+z)_{10}^{3/2}. \quad (14)$$

This suggests that  $F_0 \sim 1$  is a reasonable fiducial choice for the flux to which minihalos were exposed during reionization before overlap. In this paper we present results for  $F_0 = 1$  only. We defer the study of the effects of varying  $F_0$  to the companion paper.

## 2.3 Minihalo Strömgren numbers and I-front trapping

### 2.3.1 I-front trapping

For a spherical H II region in a uniform interstellar gas, the early expansion phase of the weak, R-type I-front ends when the I-front decelerates to twice the sound speed of the ionized gas, at which point it makes the transition from R-critical to D-critical, preceded by a shock front (Spitzer 1978). This transition occurs when the radius of the I-front approaches that of the Strömgren sphere. By analogy, we expect our intergalactic, weak, R-type I-front to make a similar transition to D-type after it enters a minihalo when it slows to the R-critical speed as it travels up the density gradient inside the minihalo, a distance comparable to the Strömgren length along its path through the halo. In order to “trap” the I-front, therefore, the minihalo size must exceed this length. We can estimate the “trapping” condition as follows.

The Strömgren length  $\ell_S(r)$  at impact parameter  $r$  is given by

$$F = \int_0^{\ell_S(r)} d\ell n_e n_H \alpha_H^{(2)} \quad (15)$$

i.e. by balancing the number of recombinations with the number of ionizing photons arriving along a given LOS.<sup>3</sup> The integration in equation (15) is done along the LOS,  $n_H$  is the H number density,  $n_e$  is the electron density,  $F$  is the flux of ionizing photons,  $\alpha_H^{(2)}$  is the Case B recombination coefficient for hydrogen, and we have assumed for simplicity that only the H in the gas is ionized. We then define the “Strömgren number” for the halo as  $L_S \equiv 2r_t/\ell_S(0)$ , where  $r_t$  is the radius of the halo and  $\ell_S(0)$  is the Strömgren length for zero impact parameter. If  $L_S > 1$ , then the halo is able to trap the I-front, while if  $L_S < 1$ , the halo would be ionized quickly by the passage of the weak, R-type I-front across

<sup>3</sup> We have adapted cylindrical coordinates  $(r, x)$  in which the  $x$ -axis is the line between the source and the minihalo center, the axis of symmetry of this problem. In writing equation (15), we have assumed that the distance between the source and the minihalo is much greater than the size of the minihalo, so we can approximate the LOS as parallel to the  $x$ -axis.

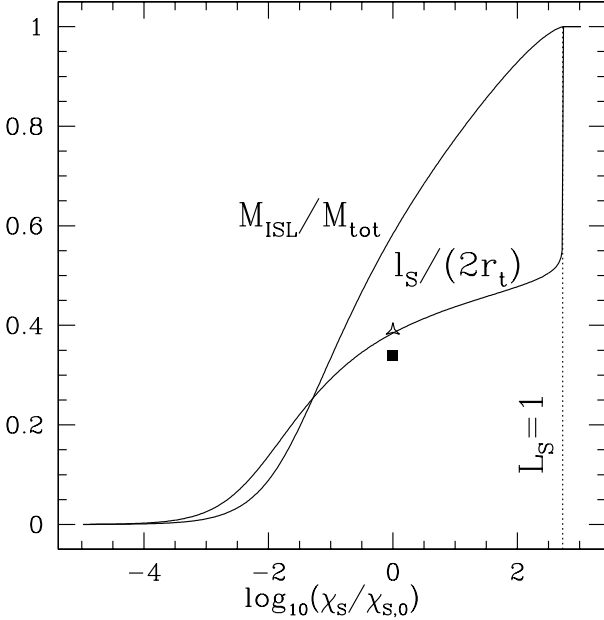


**Figure 2.** Inverse Strömgen Layer. The Strömgen length along the axis,  $\ell_S(0)$ , in units of the halo diameter  $2r_t$  and ISL mass  $M_{\text{ISL}}$  in units of the total mass  $M_{\text{tot}}$  vs.  $\chi_S/\chi_{S,0}$ , where  $\chi_S \equiv F/(\rho_0^2 r_0)$ ,  $\chi_{S,0}$  is  $\chi_S$  for our fiducial halo and  $F_0 = 1$ . Symbols indicate the (roughly) corresponding simulation results for  $M_{\text{ISL}}/M_{\text{tot}}$  (star) and  $\ell_S(0)/(2r_t)$  (square) at the moment of I-front transition from R-type to D-type (see § 5.2). Dotted line indicates the value  $\chi_{S,\text{crit}}$  for which  $L_S = 1$ . We assume  $T_4 = 2$ .

it, which will not slow down enough to be trapped. In the latter case, if  $L_S \ll 1$ , the halo gas would be uniformly photoheated to  $T \gtrsim 10^4$  K before any mass motions could occur, and the pressure gradient would blow the gas apart isotropically, long after the I-front had exited the halo.

The threshold condition  $L_S = 1$  is equivalent to

$$F = \frac{2\alpha_H^{(2)} f_b^2}{(\mu_H m_H)^2} \rho_0^2 r_0 \int_0^{\zeta_t} \bar{\rho}^2(\zeta) d\zeta, \quad (16)$$

where  $\bar{\rho} \equiv \rho/\rho_0$ ,  $\zeta \equiv r/r_0$ ,  $f_b = \Omega_b/\Omega_0$  is the baryonic mass fraction and  $\mu_H m_H$  is the mean gas mass per H atom. The dependences on the source flux and on the minihalo mass and size at different redshift are combined if we define the parameter

$$\chi_S \equiv \frac{F}{\rho_0^2 r_0} = \chi_{S,0} F_0 M_7^{-1/3} (1+z)_{10}^{-5} \left( \frac{\Omega_b h^2}{0.15} \right)^{-5/3}, \quad (17)$$

where  $M_7 \equiv M_{\text{tot}}/(10^7 M_\odot)$  and  $\chi_{S,0} \equiv 4.1 \times 10^{30} \text{ g}^{-2} \text{ cm}^3 \text{ s}^{-1}$ . We have used the fact that  $I \equiv 2 \int_0^{\zeta_t} \bar{\rho}^2(\zeta) d\zeta = 3.49$  and the scalings of  $\rho_0$  and  $r_0$  with the mass of the halo and its redshift of collapse according to the TIS model at high redshift (Iliev & Shapiro 2001). There is a direct correspondence between  $L_S$  and  $\chi_S$ , and the condition  $L_S = 1$  is equivalent to  $\chi_S = \chi_{S,\text{crit}}$  where

$$\chi_{S,\text{crit}} = 3.3 \times 10^{33} T_4^{-3/4} \left( \frac{\Omega_b h^2}{0.02} \right)^2 \times \left( \frac{\Omega_b h^2}{0.15} \right)^{-2} \text{ g}^{-2} \text{ cm}^3 \text{ s}^{-1}, \quad (18)$$

(where  $T_4$  refers to the temperature of the ionized gas) while  $L_S > 1$  and  $L_S < 1$  correspond to  $\chi_S > \chi_{S,\text{crit}}$  and  $\chi_S < \chi_{S,\text{crit}}$ , respectively. We plot  $\ell_S(0)$  vs.  $\chi_S$  in Figure 2. For our fiducial case,  $\chi_S = \chi_{S,0} \ll \chi_{S,\text{crit}}$ , so we expect the I-front to be easily trapped by the minihalo in this case. In general, the critical minihalo mass which is just large enough to trap the I-front by making  $L_S = 1$  is given by setting  $\chi_S = \chi_{S,\text{crit}}$  in equation (17) to yield

$$M_{7,\text{crit}} = 1.8 \times 10^{-9} F_0^3 [(1+z)_{10}]^{-15} T_4^{9/4} \left( \frac{\Omega_b h^2}{0.15} \right) \times \left( \frac{\Omega_b h^2}{0.02} \right)^{-6}. \quad (19)$$

For  $F_0 \lesssim 10$ , even the smallest minihalos which formed at the last possible moment before the I-front overtook them at the end of the reionization epoch at  $z_{\text{ov}} = 6$  would have been able to trap the I-front.

For a uniform halo with gas number density  $\langle n_H \rangle$ , equation (15) reduces to

$$\ell_S = \frac{F}{\alpha_H^{(2)} \langle n_H \rangle^2}. \quad (20)$$

In terms of the I-front trapping condition ( $L_S = 1$ ), a TIS halo with mean density  $\bar{\rho}_{\text{TIS}}$  is equivalent to a uniform halo of the same size but with mean density given by

$$\bar{\rho} = \rho_0 \left( \frac{I}{2\zeta_t} \right)^{1/2} = 0.24 \rho_0 = 34 \bar{\rho}_{\text{TIS}}, \quad (21)$$

where  $\bar{\rho}_{\text{TIS}}$  is the mean density of the TIS. Hence, a uniform halo of the same size as the TIS minihalo which is just large enough to trap the I-front will do so only if it is 34 times more massive than that TIS halo.

One important implication of this result is that it would be very incorrect to use the volume-average mean density of a minihalo instead of this much larger density in equation (21) to determine whether a minihalo of a given mass will trap the I-front. In particular, if we replace the realistic TIS profile of the centrally-concentrated minihalo by a uniform-density minihalo with the same mass and radius, instead, the Strömgen number,  $L_{S,\text{uniform}}$ , of this uniform halo will be very much smaller than  $L_S$  for the TIS minihalo, according to

$$L_{S,\text{uniform}} = 8.9 \times 10^{-4} (\chi_{S,\text{crit}}/\chi_S) = 0.72 M_7^{1/3} (1+z)_{10}^5 \times F_0^{-1} T_4^{-3/4} \left( \frac{\Omega_b h^2}{0.02} \right)^2 \left( \frac{\Omega_b h^2}{0.15} \right)^{-1/3}. \quad (22)$$

Hence, when a TIS minihalo of a given mass is just



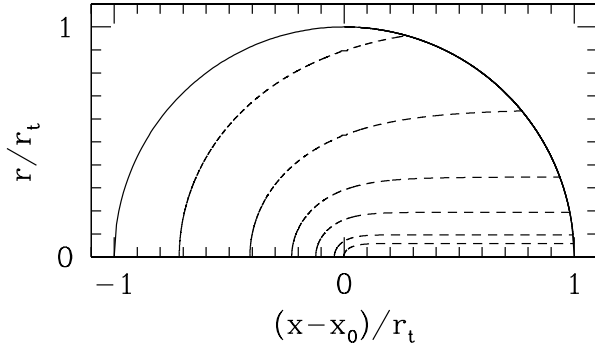


**Figure 3.** The ISL shape inside minihalo (halo boundary indicated by the solid line), according to the ISL approximation for  $\chi/\chi_{S,0} = 0.01, 0.1, 1, 10, 100$ , and  $250$  (dashed-line curves from left to right).  $x_0$  is the position of the centre of the halo along the  $x$ -axis. Both the impact parameter  $r$  and axis coordinate  $x - x_0$  are in units of the halo radius  $r_t$ . Source is located outside the box, to the left, at  $x = 0$ , where  $x_0 \gg r_t$ . We assume  $T_4 = 2$ .

marginally able to trap the I-front (i.e.  $\chi_S = \chi_{S,\text{crit}}$ ), a uniform halo with the same mass and radius has a Strömgren number  $L_S = 8.9 \times 10^{-4}$ , far below the minimum required to trap the I-front! This means that the phenomenon of I-front trapping can be missed entirely by numerical simulations of reionization which do not fully resolve the internal structure of individual minihalos, even when their resolution in mass and length are, in principle, high enough to identify minihalos of the correct mass and mean density. For this reason, the simulations we shall report here are high enough in resolution to guarantee that the internal structure of individual minihalos is fully resolved.

### 2.3.2 Inverse Strömgren Layer (ISL) in minihalo

We define the Inverse Strömgren Layer as the region inside the minihalo which is the HII region predicted by the Strömgren approximation. This region is bounded by the minihalo surface nearest to the source and by the surface defined at each impact parameter  $r$  by  $\ell_S(r)$  in equation (15). This ISL provides an estimate of the minihalo region which will be ionized first, during the weak, R-type I-front phase, and of the approximate location of the surface inside the minihalo where the transition to D-type will occur as the R-type front approaches it. In Figure 2, we show the fraction of the halo mass which is located inside the ISL,  $M_{\text{ISL}}/M_{\text{tot}}$ , vs.  $\chi_S$ , given by

$$M_{\text{ISL}} = \int_0^{r_t} 2\pi r dr \int_0^{\ell_S(r)} \rho(R) dX. \quad (23)$$

Here  $R = \{r^2 + [X - (r_t^2 - r^2)^{1/2}]^2\}^{1/2}$ . In Figure 2 we also plot  $L_S^{-1} = \ell_S(0)/(2r_t)$  (the Strömgren length for  $r = 0$  in units of the halo diameter) vs.  $\chi_S$ , and we indicate the corresponding simulation results at the approximate moment

of transition of the I-front from R-type to D-type, to be discussed in § 5.2. At  $\chi_S = \chi_{S,\text{crit}}$ , the ISL includes the entire minihalo, thus  $M_{\text{ISL}}/M_{\text{tot}} = 1$  and  $\ell_S(0) = 2r_t$ . In Figure 3, we plot the shape of the ISL surface for  $\chi_S/\chi_{S,0} = 0.01, 0.1, 1, 10, 100$ , and  $250$ . We see that, even for low values of the parameter  $\chi_S$  (equivalent to low external flux levels) a significant fraction of the halo volume becomes ionized quickly due to the relatively low density in the halo outskirts. However, from Figure 2 we see that this volume still corresponds to a small fraction of the total mass (e.g. for  $\chi_S/\chi_{S,0} < 0.01$ ,  $M_{\text{ISL}} < 10\%$ ). As  $\chi_S$  approaches  $\chi_{S,\text{crit}}$ , the neutral gas fraction shielded by the highly concentrated halo core diminishes until it disappears completely when  $\chi_S = \chi_{S,\text{crit}} = 490\chi_{S,0}$  (for  $T_4 = 2$ ).

### 2.4 Evaporation time

A rough, order-of-magnitude guide to the time-scale  $t_{\text{ev}}$  for minihalo photoevaporation is the sound-crossing time for the characteristic size of the minihalo at the sound speed of the ionized gas,  $t_{\text{sc}} = 2r_t/c_s(10^4\text{K})$ . The actual I-front propagation and evaporative wind are quite complex, as we shall see, and depend upon additional properties like the halo mass and density, flux level and spectrum, and the time it takes the halo and background universe to evolve. However, this simple estimate will be a convenient standard of reference with which to compare the actual simulation results.

For a minihalo of mass  $M$  at high redshift, we obtain

$$t_{\text{sc}} = 98 \text{ Myr } (M_7)^{1/3} \left( \frac{\Omega_0 h^2}{0.15} \right)^{-1/3} (1+z)_{10}^{-1}, \quad (24)$$

using the adiabatic sound speed  $c_s(10^4\text{K}) = 11.7(T_4/\mu)^{1/2} = 15.2 T_4^{1/2} \text{ km s}^{-1}$ , where  $\mu = 0.59$  is the mean molecular weight for fully ionized gas of H and He if the abundance of He is  $A(\text{He}) = 0.08$  by number relative to H, and we have assumed  $T_4 = 1$ . Of course, if  $t_{\text{ev}} \geq t_H$ , the Hubble time at the epoch of photoevaporation, then the underlying properties of the halo, infall, ionizing source, and background universe will evolve significantly during the process. The Hubble time at high redshift in the  $\Lambda\text{CDM}$  universe is

$$t_H = \frac{2}{3H(z)} \approx 533 \text{ Myr } \left( \frac{\Omega_0 h^2}{0.15} \right)^{-1/2} (1+z)_{10}^{-3/2}. \quad (25)$$

Thus, the ratio of the two timescales is

$$\frac{t_{\text{sc}}}{t_H} = 0.184 (M_7)^{1/3} \left( \frac{\Omega_0 h^2}{0.15} \right)^{1/6} (1+z)_{10}^{1/2}. \quad (26)$$

We see that this ratio is only weakly dependent on the background cosmology, and suggests that the photoevaporation of a minihalo over the range of mass and epochs of interest will be completed in less than a Hubble time, if this estimate of  $t_{\text{ev}}$  is correct.

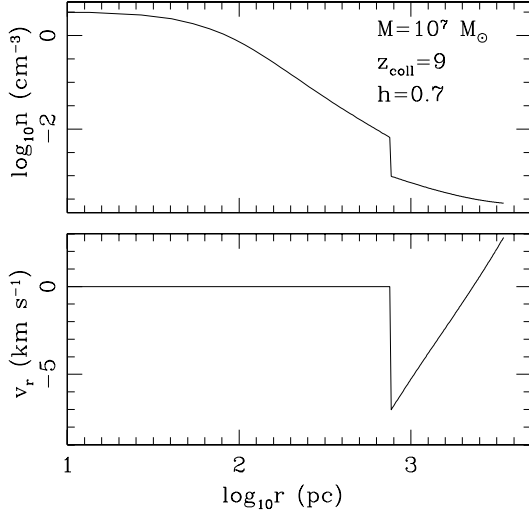


**Figure 4.** Initial conditions for the minihalo photoevaporation simulations (TIS halo + self-similar cosmological infall): atomic number density (upper panel), and radial velocity (lower panel) profiles vs. radius for minihalo of mass  $M_7 = 1$  at  $(1+z)_{10} = 1$ .

## 2.5 Ionizing photon consumption

An important quantity characterizing the effect of minihalos on the process of reionization is the consumption of ionizing photons which results from photoabsorption by minihalo atoms during their photoevaporation. We can parametrize this consumption by the photon-to-atom ratio,  $\xi \equiv N_\gamma/N_a$ , i.e. how many photons per minihalo atom are required to photoevaporate the halo. Collapsed minihalos are significantly denser than the IGM, thus the recombination rate inside is significantly higher, leading to a much higher photon consumption rate per unit time per atom, which could in turn have a substantial effect on the progress and duration of reionization.

We define the effective absorption cross-section at frequency  $\nu$  of a minihalo at a given time  $t$  as

$$\sigma_{\text{eff},\nu}(t) \equiv \int_0^\infty 2\pi r [1 - e^{-\tau_\nu(r,t)}] dr, \quad (27)$$

where  $\tau_\nu = \tau_{\nu,\text{H}} + \tau_{\nu,\text{He I}} + \tau_{\nu,\text{He II}}$  is the total bound-free opacity at impact parameter  $r$  and time  $t$ , including the minihalo gas which is leaving the halo in a wind, where

$$\tau_i(r,t) = \int_{\nu_{\text{th},i}}^\infty \sigma_{\text{bf},i}(\nu) n_i d\nu. \quad (28)$$

where  $\sigma_{\text{bf},i}$  and  $\nu_{\text{th},i}$  are the bound-free cross-section and ionization threshold frequency and  $n_i$  is the number density for species  $i$ . The number of photons absorbed by the minihalo gas per minihalo atom over time  $t_{\text{ev}}$  is then given by

$$\xi_\tau = \frac{1}{N_a} \int_0^{t_{\text{ev}}} \int_{\nu_H}^\infty F_\nu(t) \sigma_{\text{eff},\nu}(t) d\nu dt, \quad (29)$$

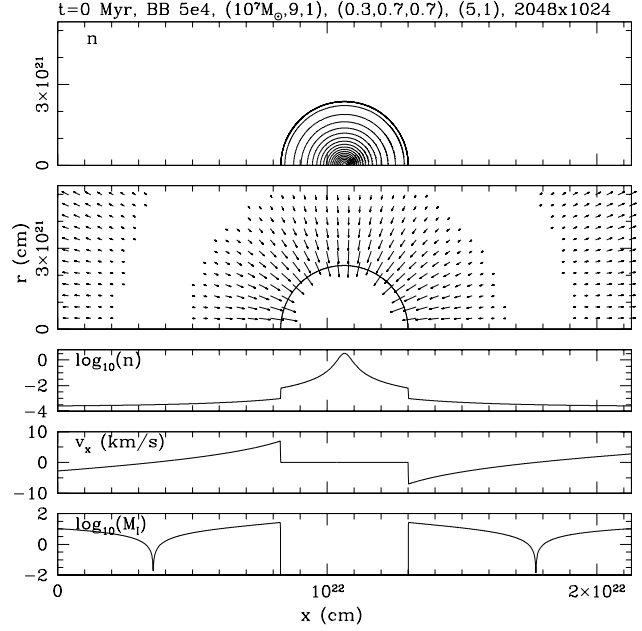


**Figure 5.** Initial time-slice at  $t = 0$  Myrs ( $z = 9$  in  $\Lambda$ CDM universe), from top to bottom: (1) isocontours of atomic density, logarithmically spaced, in  $(r, x)$ -plane of cylindrical coordinates; (2) flow velocities; arrows are plotted with length proportional to gas velocity. An arrow of length equal to the spacing between arrows has velocity  $5 \text{ km s}^{-1}$ ; the minimum velocities plotted are  $1 \text{ km s}^{-1}$ . Solid line indicates the boundary of the minihalo; cuts along the  $r = 0$  axis of: (3) gas number density  $n$ , (4) velocity  $v_x$ , and (5) Isothermal Mach number  $M_I$ . Source is located outside the box, far to the left along the  $x$ -axis.

where  $F_\nu(t)$  is the time dependent ionizing photon flux per unit frequency.

Alternatively,  $\xi$  can be calculated by the direct count of the number of recombinations experienced by each atom which was initially in the halo:

$$\xi_{\text{rec}} = 1 + \frac{1}{N_a} \int_0^{t_{\text{ev}}} dt \int dV (\alpha_H^{(2)} n_e n_{\text{H II}} + \alpha_{\text{He}}^{(2)} n_e n_{\text{He II}}), \quad (30)$$

where  $n_e$  is the number density of electrons,  $n_{\text{H II}}$  and  $n_{\text{He II}}$  are the number densities of H II and He II, and  $\alpha_H^{(2)}$  and  $\alpha_{\text{He}}^{(2)}$  are the Case B recombination coefficients for H II and He II, respectively, and the volume integral is over all Lagrangian fluid elements initially inside the minihalo when the I-front first encountered it. We have neglected the recombinations of He III to He II because these generally contribute diffuse flux which is absorbed on-the-spot by H and He.

A naïve estimate of  $\xi$  is obtained if we assume that the minihalo is optically-thin and instantaneously ionized but remains static at its initial density for a time  $t_{\text{sc}}$ . Then, ignoring the contribution of He to recombinations, equation (30) yields

$$\xi = f \frac{C_{\text{int}} \langle n_H \rangle \alpha_H^{(2)}}{1 + \delta_{\text{TIS}}} t_{\text{sc}} \quad (31)$$

(Haiman, Abel & Madau 2001), where  $\langle n_H \rangle$  is the mean H atom number density inside a halo,  $C_{\text{int}} \equiv \langle n_H^2 \rangle / \langle n_H \rangle^2 = 444^2$  is the effective clumping factor for the TIS, and  $1 + \delta_{\text{TIS}} = 130.6$  is the average overdensity of a TIS halo with respect to the cosmic mean background density. Since, in reality, such a model is oversimplified, we also introduce an “efficiency” factor  $f$  which we will derive from our simulations below. Thus we obtain

$$\xi = 206 f T_4^{-3/4} M_7^{1/3} \left( \frac{\Omega_0 h^2}{0.15} \right)^{-1/3} (1+z)_{10}^{-1}. \quad (32)$$

According to this estimate, if  $f \approx 1$  as claimed by Haiman, Abel & Madau (2001), based on their simulation of a uniformly-ionized minihalo with zero optical depth, the photoevaporation of minihalos can be an enormous sink of ionizing photons during the reionization epoch. By contrast, atoms in the IGM at closer to the mean baryon density have otherwise been estimated previously to consume only  $\xi \sim 1$  photons per atom during reionization (Gnedin 2000; Miralda-Escude, Haehnelt & Rees 2000). It is crucial, therefore, for us to perform the detailed simulations reported here in order to derive the efficiency factor  $f$  in equation (32) properly.

### 3 THE CALCULATION

#### 3.1 Basic equations

##### 3.1.1 Gas dynamical conservation equations

We solve the Eulerian conservation equations of fluid dynamics for the vector  $\mathbf{U}$  of the densities of conserved quantities in 2-D, cylindrical symmetry,

$$\mathbf{U} = (\rho, \rho v_x, \rho v_r, E, n_{i,z}), \quad (33)$$

mass density  $\rho$ , momentum densities  $\rho v_x$  in the  $x$ -direction and  $\rho v_r$  in the radial direction, energy density  $E = \rho(v_x^2 + v_r^2)/2 + \epsilon$  and number density of chemical species  $i$  in ionization stage  $z$ ,  $n_{i,z}$ . Here  $v_x$  and  $v_r$  are the velocity components,  $\epsilon = c_V T$  is the specific internal energy,  $T$  is the temperature and  $c_V$  is the isochoric specific heat. The Eulerian conservation equations can then be written as

$$\frac{\partial \mathbf{U}}{\partial t} + \frac{\partial \mathbf{F}(\mathbf{U})}{\partial x} + \frac{\partial \mathbf{G}(\mathbf{U})}{\partial r} = \mathbf{S}, \quad (34)$$

where  $\mathbf{F}(\mathbf{U})$  and  $\mathbf{G}(\mathbf{U})$  are the fluxes of  $\mathbf{U}$  in the  $x$  and  $r$  directions, respectively, given by:

$$\mathbf{F}(\mathbf{U}) = (\rho v_x, \rho v_x^2 + p, \rho v_x v_r, v_x(E + p), n_{i,z} v_x), \quad (35)$$

and

$$\mathbf{G}(\mathbf{U}) = (\rho v_r, \rho v_x v_r, \rho v_r^2 + p, v_r(E + p), n_{i,z} v_r), \quad (36)$$

and  $\mathbf{S}$  are the source terms:

$$\mathbf{S} = \left[ -\frac{\rho v_r}{r}, -\frac{\rho v_x v_r}{r} - (\nabla \phi)_x, -\frac{\rho v_r^2}{r} - (\nabla \phi)_r, \right.$$

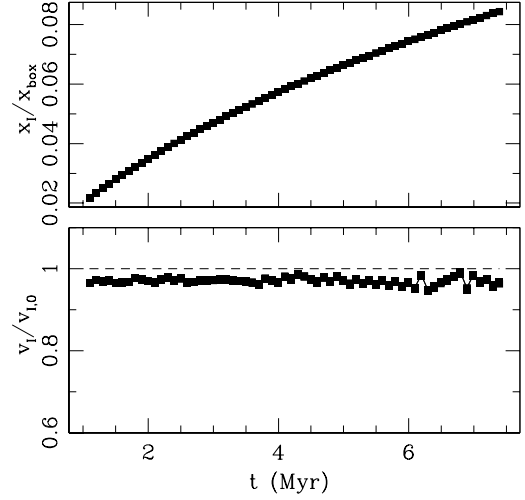


**Figure 6.** R-type I-front speed. Position  $x_I$  (in units of the box length  $x_{\text{box}} = 5.64$  Mpc; upper panel) and velocity  $v_I$  (in units of the analytical prediction as described in the text; lower panel) of an R-type ionization front propagating through the mean IGM at redshift  $z = 9$ .

$$-\frac{v_r(E + p)}{r} - \mathbf{v} \cdot \nabla \phi - \Lambda + \Gamma, -\frac{n_{i,z} v_r}{r} + S_{i,z} \Big]. \quad (37)$$

Here  $p$  is the pressure,  $\phi$  is the gravitational potential,  $\Lambda$  is the cooling rate,  $\Gamma$  is the heating rate, and  $S_{i,z}$  is the source function for the chemical species  $i$  in ionization stage  $z$ , as described in § 3.1.2. We use the ideal gas equation of state for monatomic gas ( $\gamma = 5/3$ )

$$p = \frac{1}{\gamma - 1} \epsilon \rho. \quad (38)$$

##### 3.1.2 Nonequilibrium chemical reaction network

We take account of the nonequilibrium ionization balance of H, He, and a possible admixture of heavy elements C, N, O, Ne, and S, as described in Raga et al. (1997), Mellema et al. (1998), and references therein. [For a description of the details and checks of our microphysics, the reader is referred to Mellema (1993)].

The source function for the nonequilibrium chemical reaction network is given by

$$S_i = n_e n_{i,z+1} \alpha_{i,z+1}(T) + n_e n_{i,z-1} C_{i,z-1} - n_e n_z \alpha_{i,z}(T) - n_e n_{i,z} C_{i,z} + n_{i,z-1} \phi_{i,z-1} - n_{i,z} \phi_{i,z}, \quad (39)$$

where, as above,  $i$  labels the chemical elements,  $z$  labels the ionization state,  $\alpha_{i,z+1}(T)$  is the recombination rate from stage  $z + 1$  to  $z$ ,  $C_{i,z-1}$  is the collisional ionization rate from  $z - 1$  to  $z$ ,  $\phi_{i,z} = \int_{\nu_{\text{th},i}}^{\infty} (F_{\nu} \sigma_{\nu,i,z}) / (h\nu) d\nu$  is the photoionization rate from  $z$  to  $z + 1$ , and  $\nu_{\text{th},i}$  is the photoionization threshold for species  $i$ . Charge exchange reactions are included, although we have not displayed them in equa-

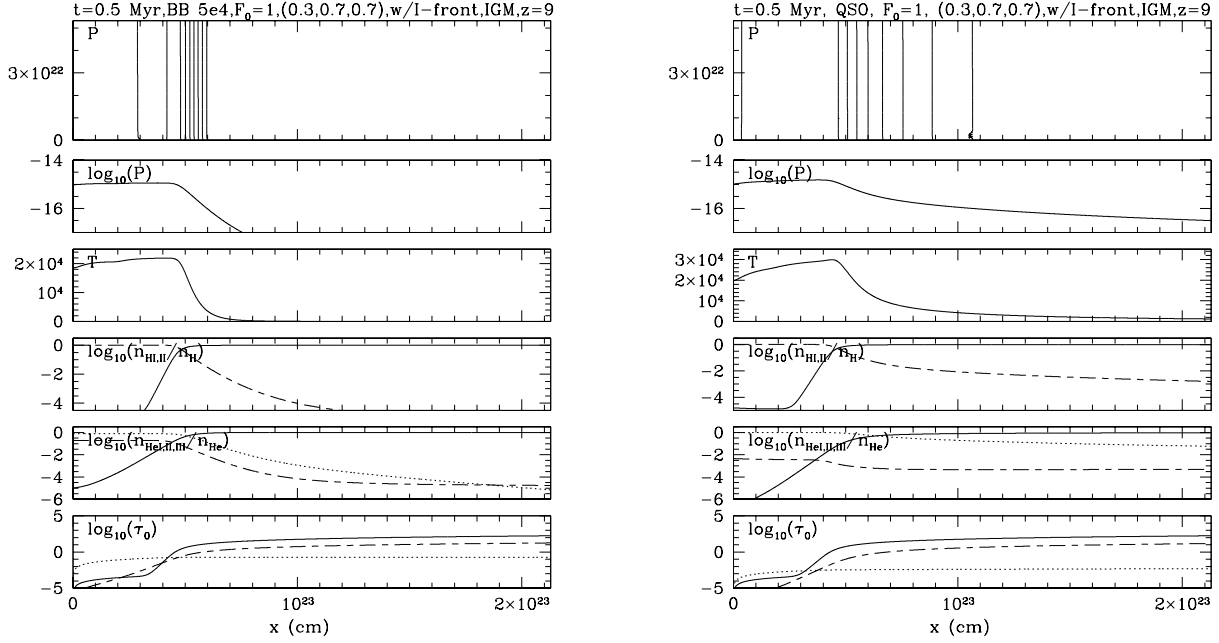


**Figure 7.** Detailed structure of R-type ionization front in the mean IGM at  $z = 9$  at time 0.5 Myr after the ionizing flux turns on at the left-side boundary of the box. (a) (left) BB 5e4 case and (b) (right) QSO case. From top to bottom: (1) isocontours of pressure, logarithmically spaced, in  $(r, x)$ -plane of cylindrical coordinates; cuts along the  $x$ -axis (the I-front propagation direction) of (2) pressure, (3) temperature  $T$ , (4) H I (solid) and H II (dotted) fractions; (5) He I (solid), He II (dashed) and He III (dotted) fractions; (6) bound-free optical depths measured from  $x = 0$  along the  $x$ -axis, for H I (solid), He I (dashed), and He II (dotted) at their respective ionization thresholds. Source is located 0.5 Mpc, to the left of the box.

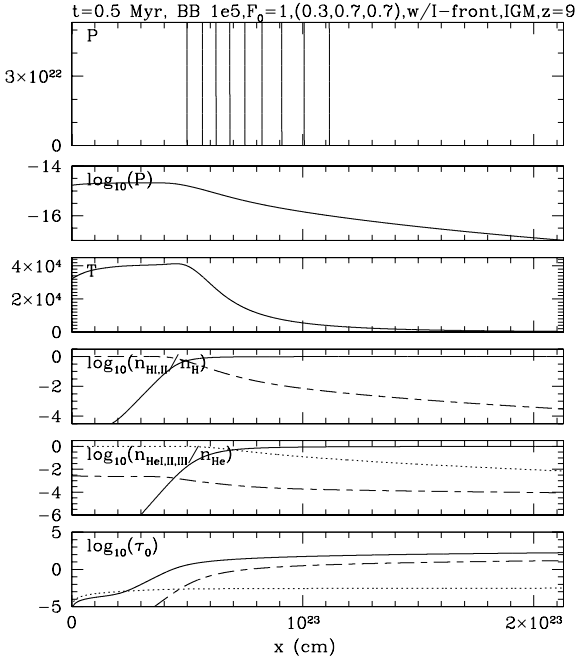


**Figure 8.** Same as in Figure 7, but for BB 1e5 case.

tion (39). Recombination rates include radiative and dielectronic rates.

The electron number density  $n_e$  is given by  $n_e = n_{\text{H II}} + n_{\text{He II}} + 2n_{\text{He III}} + n_{\text{C}}$ . The contribution of one electron per carbon atom is added to ensure that the electron number density is always positive. Since the ionization threshold of carbon is below 13.6 eV and the IGM is transparent to these photons even before reionization, C is always at least singly ionized. The contribution of the other metals to the electron density is assumed negligible.

### 3.1.3 Radiative cooling and photo-heating

Our nonequilibrium cooling function includes collisional line excitation and ionization, recombination and free-free cooling due to H, C, N, O, Ne, and S, as described and tested in detail in Raga et al. (1997), to which we have added He cooling and the Compton cooling which results from inverse Compton scattering of the CMB photons off free electrons. The Compton cooling rate is given by

$$\Lambda_{\text{Comp}} = 5.65 \times 10^{-36} n_e (1+z)^4 (T - T_{\text{CMB}}) \text{ erg cm}^{-3} \text{ s}^{-1} \quad (40)$$

(Shapiro & Kang 1987), where  $T_{\text{CMB}} = 2.73(1+z)$  is the CMB temperature at redshift  $z$ ,  $n_e$  is the local density of free electrons, and  $T$  is the local gas temperature.

The photo-heating rate  $\Gamma$  (in units of  $\text{erg cm}^{-3}\text{s}^{-1}$ ) is the sum of the ionization heating terms for each of the species H I, He I, and He II:

$$\Gamma_{i,z} = n_{i,z} \int_{\nu_{\text{th},i,z}}^{\infty} \frac{F_{\nu}(h\nu - h\nu_{\text{th},i,z})}{h\nu} \sigma_{\text{bf},\nu,i,z} d\nu. \quad (41)$$

### 3.1.4 Radiative transfer and the ionizing flux

The energy flux of ionizing photons at a point with coordinates  $(r, x)$  for a source on the  $x$ -axis at position  $x_0$  is given by

$$F_{\nu}(r, x) = \frac{L_{\nu}}{4\pi [r^2 + (x - x_0)^2]} e^{-\tau_{\nu}(r, x)}. \quad (42)$$

Here  $L_{\nu}$  is the source luminosity at frequency  $\nu$ , and  $\tau_{\nu}(r, x)$  is the bound-free optical depth from the source to the point  $(r, x)$ , given by

$$\tau_{\nu}(r, x) = \sigma_{\nu, \text{HI}} N_{\text{HI}} + \sigma_{\nu, \text{HeI}} N_{\text{HeI}} + \sigma_{\nu, \text{HeII}} N_{\text{HeII}}, \quad (43)$$

where  $N_{i,z}$  is the column density of species  $i$  at ionization stage  $z$  along the line from the source to the point  $(r, x)$ .

### 3.1.5 Gravity force

We have modified the code to include the gravity field due to the halo of dark matter and gas, and the infalling matter, as discussed in detail in the Appendix. We neglected the small change in this gravity force over time which results from the gas dynamical evolution which moves the gas relative to the dark matter. Thus the density field used for the gravity calculation is spherically-symmetric at all times and the gravitational acceleration is given by

$$a_{\text{grav}} = -\nabla\phi = \frac{GM(\leq R)}{R^2}, \quad (44)$$

where  $M(\leq R)$  is the time-varying mass within the spherical radius  $R = (r^2 + x^2)^{1/2}$ . This force is included in the Euler equations (34) through the source term  $\mathbf{S}$  as shown in equation (37).

## 3.2 Initial conditions

### 3.2.1 Minihalo and cosmological infall

As discussed above, the halo in our illustrative simulations has radius  $r_t = 0.76$  kpc, and virial temperature  $T_{\text{vir}} = 4000$  K, corresponding to dark-matter velocity dispersion  $\sigma_v = 5.2 \text{ km s}^{-1}$ . The initial number density and velocity profiles of the halo and the infall are shown in Figure 4. For comparison with our simulation results at later times, we show the initial conditions on the computational grid in Figure 5 (top to bottom): (1) the density contours (logarithmically-spaced), (2) the initial velocity field, and cuts along the axis of: (3) gas number density  $n$ , (4) velocity  $v_x$ , and (5) Isothermal Mach number  $M_I \equiv v/c_{s,I}$ , where  $c_{s,I}$  is the isothermal sound speed. The computational box

is chosen so that the turn-around radius of the cosmological infall starts well inside the box. This ensures that the gas next to the simulation boundaries (excluding the axis of symmetry) is outflowing throughout the simulation, consistent with our transmissive numerical boundary conditions (see § 4).

### 3.2.2 Source spectra and evolution

The source is on the axis of symmetry, far away (thus the rays are close to parallel, although the code actually takes the true angles properly into account) to the left of the box. We consider three possible spectra as described in § 1, two stellar cases, black-body spectra with effective temperatures  $T = 50,000$  K (“BB 5e4”) for Pop. II stars and  $T = 10^5$  K (“BB 1e5”) for Pop. III stars, and a power-law QSO-like energy spectrum with index  $\alpha = -1.8$ . As the universe expands, the proper distance between the source and the minihalo grows, as  $x_0(t) \propto a(t)$ , where  $a(t)$  is the cosmic scale factor, so the incident flux level decreases  $\propto x_0^{-2} \propto a(t)^{-2}$ .

### 3.2.3 R-type I-front encounters the simulation volume at $t = 0$

The I-front has a finite width of  $\sim (10-20)$  mean free paths. For the intergalactic weak, R-type I-front which encounters the minihalo, this mean free path in the IGM is a few kpc, which is similar to our simulation box size. Therefore, it would be inaccurate to start the simulations by assuming a sharp I-front at the left box boundary. Instead, we start our simulations shortly before the I-front arrival at the left boundary, as follows. We assume the the gas outside the box is uniform, at the mean IGM density, for which case there is an exact solution for the weak, R-type I-front propagation. We then use the frequency-dependent optical depths given by the current position of the I-front obtained from the analytical solution to attenuate the spectrum of the photoionizing source which enters the computational box. While not exact (e.g. due to infall which slightly increases the local density around the halo) this approach closely imitates the gradual rise in the photoionizing radiation flux arriving from the source as the I-front approaches and the hardening of the spectrum due to the deeper penetration of higher-energy photons. As an alternative, it is also possible to take a much larger simulation box, which would allow the I-front to relax to its correct structure before arriving at the halo. However, such an approach would either degrade the resolution unacceptably, or else the simulation would become prohibitively (and needlessly) more expensive.

## 4 NUMERICAL METHOD AND TESTS

### 4.1 The method

We use a 2-D axisymmetric Adaptive Mesh Refinement (AMR) code (called CORAL) described in detail in

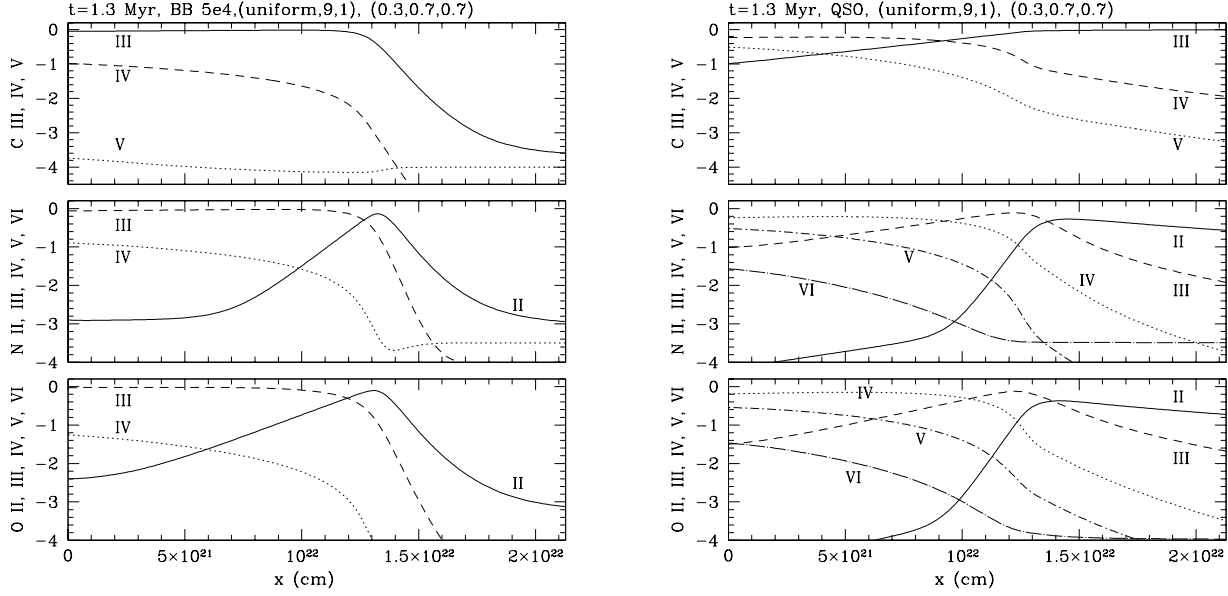


**Figure 9.** Ionization structure of metals in R-type I-front propagating in the mean IGM at  $z = 9$ , 1.3 Myr after front enters the box on the left-hand-side. C, N, and O ionic fractions along symmetry axis: (a) (left) BB 5e4 case; (b) (right) QSO case.

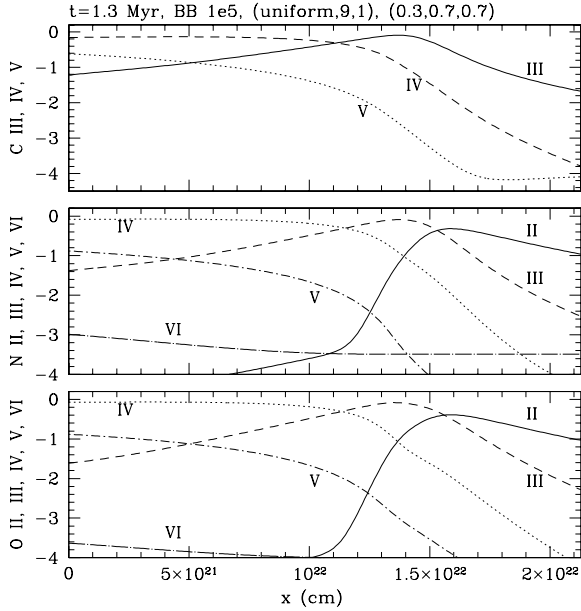


**Figure 10.** Same as in Figure 9, but for BB 1e5 case.

Raga et al. (1995) and Mellema et al. (1998). The code has been extensively tested and applied to a range of problems including simulations of Herbig-Haro jets and the photoevaporation of uniform density interstellar clouds near plan-

etary nebulae. Here we will discuss the numerical details of the code only briefly, concentrating on the new elements in the code introduced by us, and we refer the reader to these earlier papers and references below for a more in-depth discussion.

The numerical scheme for solving the Euler equations is an adaptive grid implementation of the van Leer Flux Vector Splitting method (van Leer 1982), improved to second order accuracy by use of linear gradients within cells as described in Arthur (1991). The refinement and de-refinement criteria are based on the gradients of all code variables. When the gradient of any variable is larger than a pre-defined value the cell is refined, while when the criterion for refinement is not met the cell is de-refined. We have modified the code to include the gravitational acceleration in equation (44), as discussed in detail in the Appendix. We impose reflective boundary conditions on the axis and transmissive boundary conditions on the other three boundaries of the box.

The code timestep is set in general by the minimum of the timesteps determined by the Courant condition, the ionization time scale and gravity,

$$\Delta t = \min(\epsilon_{\text{Cour}} \Delta t_{\text{Cour}}, \epsilon_{\text{ion}} \Delta t_{\text{ion}}, \epsilon_{\text{grav}} \Delta t_{\text{grav}}). \quad (45)$$

The Courant time in equation (45) is

$$\Delta t_{\text{Cour}} = \Delta x / c_s, \quad (46)$$

where  $\Delta x$  is the cell width. The ionization time scale here is that for ionizing hydrogen,

$$\Delta t_{\text{ion}} = \epsilon_{\text{ion}} \frac{n_{\text{HI}}}{(dn_{\text{HI}}/dt)} = \epsilon_{\text{ion}} \frac{n_{\text{HI}}}{|n_{\text{HI}} \phi_{\text{HI}} - n_{\text{HII}}^2 \alpha_{\text{H}}^{(2)}|}, \quad (47)$$

where  $\phi_{HI}$  is the photoionization rate for hydrogen,  $n_{HI}$  and  $n_{HII}$  are the number densities of neutral and ionized hydrogen,  $\alpha_H^{(2)}$  is the Case B recombination coefficient for hydrogen, and  $\epsilon_{ion}$  is a constant to be determined. The gravity time is just

$$\Delta t_{grav} = (\Delta x / a_{grav})^{1/2}. \quad (48)$$

The constants  $\epsilon_i$  are small numbers whose values are chosen to ensure accuracy and stability while minimizing the total number of timesteps per simulation. In all cases considered here, the timestep is set by the Courant condition, except when the fast, R-type I-front propagates through the computational box. In the latter case, the ionization time scale is smaller than the Courant time, and the value of  $\epsilon_{ion}$  is chosen by experimentation to optimize the accuracy and efficiency of the test problem described in § 4.3. For the Courant condition, the van Leer Flux Vector Splitting scheme is stable when  $\epsilon_{Cour} \leq [2\gamma + M(3 - \gamma)]/(\gamma + 3)$ , where  $\gamma = 5/3$  is the adiabatic index and  $M$  is the Mach number. For  $M = 0$  we obtain the condition  $\epsilon_{Cour} \leq 5/7$  for the scheme to be stable for any Mach number  $M$ . For the current simulations we utilized the conservative value  $\epsilon_{Cour} = 0.4$ .

The microphysical processes – chemical reactions, radiative processes, transfer of radiation, heating and cooling – are implemented though the standard approach of operator-splitting (i.e. solved each time-step, side-by-side with the hydrodynamics and coupled to it through the energy equation). The energy and chemical rate equations are solved semi-implicitly. We follow the nonequilibrium evolution of the ionic species of H, He, C II–VI, N I–VI, O I–VI, Ne I–VI, and S II–VI. The species C I and S I are assumed fully ionized since their ionization thresholds are below the ionization threshold of hydrogen and the gas is largely optically-thin to such low energy photons [for details see Mellema et al. (1998) and references therein]. The method for solving the nonequilibrium chemistry equations is from Schmidt-Voigt & Koeppen (1987) and is implemented as described and tested in Raga et al. (1997) and Mellema et al. (1998). We use Case B recombination coefficients and the corresponding cooling rates, as is appropriate for the range of densities and temperatures in these simulations.

Radiative transfer of the ionizing photons is treated explicitly by taking into account the bound-free opacity of H and He in the photoionization rates and heating rates as explained in detail in Mellema et al. (1998). In order to speed up the radiative transfer calculation, the optical depths are approximated as described in Tenorio-Tagle et al. (1983), as follows:

$$\tau_\nu = \begin{cases} \tau_{\nu,A} & \text{for } \nu_{th,HI} \leq \nu \leq \nu_{th,HeI} \\ \tau_{\nu,B} & \text{for } \nu_{th,HeI} \leq \nu \leq \nu_{th,HeII} \\ \tau_{\nu,C} & \text{for } \nu_{th,HeII} \leq \nu, \end{cases} \quad (49)$$

where

$$\tau_{\nu,A} = \tau_{\nu,HI} \left( \frac{\nu}{\nu_{th,HI}} \right)^{-2.8}, \quad (50)$$

$$\tau_{\nu,B} = [(0.63)^{1.7} \tau_{\nu,HI} +$$

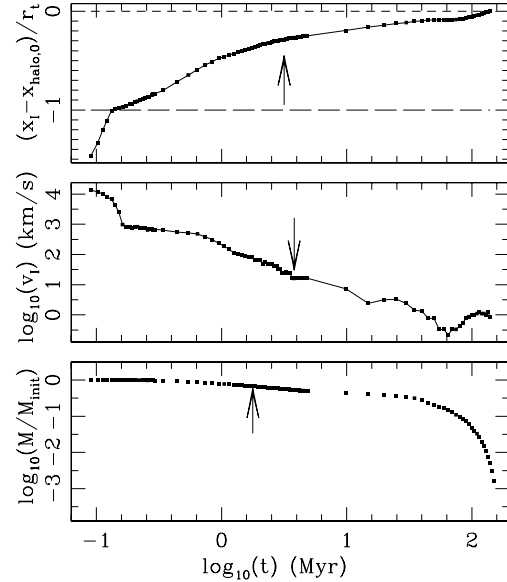


**Figure 11.** Evolution of the I-front from R-type to D-type inside the minihalo for BB 5e4 case. (upper panel) Position  $x_I$  (relative to minihalo center, in units of the minihalo radius  $r_t$  at  $t = 0$ ) and (middle panel) velocity  $v_I$  of the I-front as it travels toward and across the minihalo. The positions of the halo boundary (long-dashed line) and centre (short-dashed line) are also indicated. (lower panel) Fraction of mass  $M_{init}$ , the mass which is initially inside the minihalo when the intergalactic I-front overtakes it, which remains neutral versus time  $t$ . The arrows in the top and bottom panels mark the analytically-calculated width of the ISL for zero impact parameter and the mass fraction inside the ISL, respectively, while the arrow on middle panel marks the moment when I-front becomes R-critical, defined by the condition  $v_I = 2c_{s,I,2}$ , the onset of transition from R-type to D-type, where  $c_{s,I}$  is isothermal sound speed of ionized, post-front gas.

$$+ (1.81)^{1.7} \tau_{\nu,HeI} \left( \frac{\nu}{\nu_{th,HI}} \right)^{-1.7}, \quad (51)$$

and

$$\tau_{\nu,C} = [\tau_{\nu,HI} + (2.73)^{2.8} \tau_{\nu,HeI} + 4^{2.8} \tau_{\nu,HeII}] \left( \frac{\nu}{\nu_{th,HI}} \right)^{-2.8}. \quad (52)$$

Here  $\tau_{\nu,i,z} = \sigma_{\nu,th,i,z} N_i$  are the optical depths at the respective ionization thresholds of H I, He I and He II. This allows us to precompute the integrals over frequency involved in calculating photoionization and photoheating rates for each assumed source spectrum to make an extensive look-up table for these rates as functions of the threshold optical depths, for use in the rapid computation of these rates during each run by interpolation between entries in the look-up table. In order to speed up the calculations further, the optical depths are normally re-calculated once every 5 time steps.

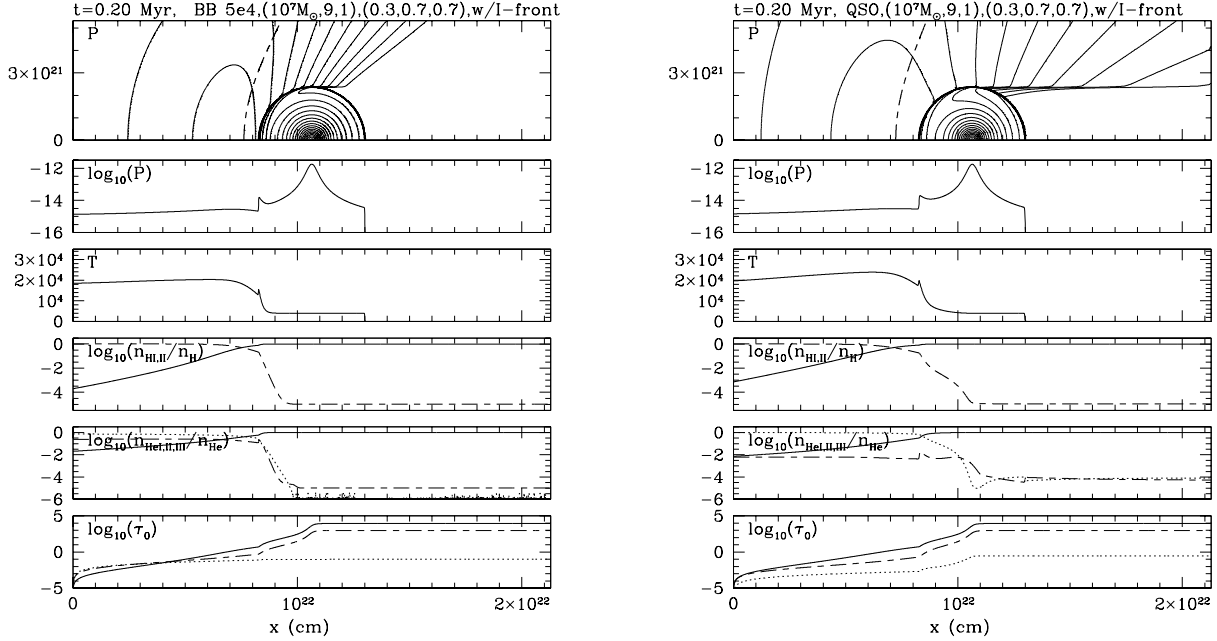


**Figure 12.** Weak, R-type phase of I-front in IGM just about to overtake a  $10^7 M_\odot$  minihalo at  $z = 9$ ,  $t = 0.2$  Myr after the I-front entered the box at left-hand side (ionizing source is located far to the left of computational box along the  $x$ -axis): (a) (left) BB 5e4 case and (b) (right) QSO case. Panels show the same quantities as in Figure 7. The current position of the I-front (50 % ionization level of hydrogen) is indicated on the uppermost panel with the dashed line.

## 4.2 Simulation parameters

Our box size in  $(r, x)$  dimensions is  $3.45 \text{ kpc} \times 6.9 \text{ kpc}$ , except for the uniform IGM simulations in § 4.3 and § 5.1, where we adopted larger boxes, as described there. The resolution at the finest grid level (i.e. fully-refined) is  $1024 \times 2048$  cells, again with the exception of the simulations in § 4.3 and § 5.1, where such high resolution was not required, but a longer propagation time was necessary, so we used resolutions of  $64 \times 8192$  and  $512 \times 1024$ , respectively.

The gas consists of hydrogen and helium in primordial abundance (24.2 % He by mass), with a small trace of metals (C, N, O, Ne, and S) at  $10^{-3} Z_\odot$ . The initial ionizing flux we adopt is  $F_0 = 1$ , except in § 4.3 where we use  $F_0 = 4$ . Each photoevaporation simulation took from several days to 1 week on a 2 GHz Athlon processor.

## 4.3 Test problem: R-type I-front in uniform IGM

In order to track properly the supersonic, weak, R-type I-fronts which sweep into and around our minihalos, we defined an “ionization time-step” related to the time-scale for ionizing hydrogen, as described above in § 4.1. We tested the scheme and adjusted the value of  $\epsilon_{\text{ion}}$  by performing a simulation of an ionization front propagating through a uniform density IGM in a long and thin ( $44 \text{ kpc} \times 5.64 \text{ Mpc}$ ), quasi-1D simulation box at resolution  $64 \times 8192$ . In this case, the gas is pure hydrogen, so there is a well-known exact analytical solution for the I-front propagation (Shapiro & Giroux

1987). The density of the gas is equal to the mean cosmic baryon density at  $z = 9$ . The source is located on the symmetry axis, 0.5 Mpc to the left of the computational box, with a flux as measured at the left boundary of the box equal to  $F_0 = 4$ . At time  $t = 0$ , the box is neutral. We identify the location of the I-front as the position at which the ionized fraction is  $x = 0.5$ . The result is plotted in Figure 6. By experiment, we found that  $\epsilon_{\text{ion}} = 0.05$  is sufficient to obtain the correct velocity for the R-type I-front to better than 5 %, as shown in Figure 6. Using larger  $\epsilon_{\text{ion}}$  can lead to an underestimate of the velocity by a significant amount.

## 5 RESULTS

### 5.1 Structure of global I-front in the IGM during reionization: the weak, R-type phase

To study the detailed temperature and ionization structure of the global I-front during reionization in its weak, R-type phase and the dependence of these on the source spectrum, we performed a set of three simulations of an I-front in the uniform IGM at  $z = 9$ , by “zooming in” with a smaller box ( $34.5 \text{ kpc} \times 69 \text{ kpc}$ ) and better length resolution ( $512 \times 1024$ , fully-refined) than were used in the test problem in the previous section. The source in each case produced a flux  $F_0 = 1$  at the left boundary of the simulation box, with a different spectrum for each simulation. The results are shown in Figures 7–10. As expected, for the cases with harder spectra



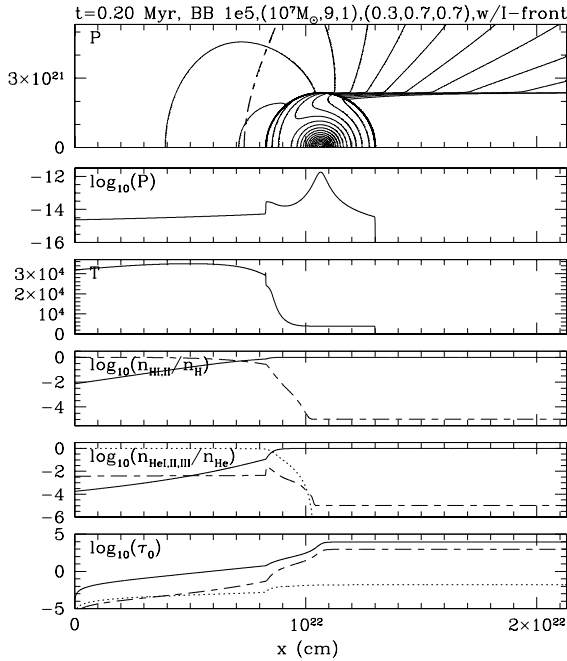


**Figure 13.** Same as Figure 12, but for BB 1e5 case.

(i.e. QSO, BB 1e5), the I-front is broader than in the case BB 5e4, due to the more deeply penetrating hard photons of the former cases. There is significant pre-heating and pre-ionization in the former cases, ahead of the point inside the I-front at which the H neutral fraction is 0.5. In all cases, the ionization of He is predominantly from He I on the neutral side to He III on the ionized side, with only a small fraction of He II. The position of the hydrogen I-front ( $x_H = 0.5$ ) is nearly coincident with the corresponding point for helium ( $x_{He} = 0.5$ ) for the softer BB 5e4 spectrum, while for the harder QSO and BB 1e5 spectra the He I-front is more advanced by  $\sim 7$  kpc. Another important difference to note is that the post-front temperature is  $\sim 2 \times 10^4 K$  in the BB 5e4 case, but  $\sim 3 \times 10^4 K$  in the QSO case, and even higher,  $\sim 4 \times 10^4 K$  in the BB 1e5 case. The ionization states of the trace of heavier elements also differ significantly for different source spectra, as shown in Figures 9 and 10. The BB 5e4 spectrum ionizes C, N, and O mostly to C III, N III, and O III, respectively, with only small fractions, of order 10 %, of C IV, N IV, and O IV, while the BB 1e5 spectrum ionizes these species mostly up to ionization stage IV, with a notable fraction ( $> 10\%$ ) of ionization stage V, and tiny fractions of O VI and N VI. Finally, the hard QSO spectrum is able also to produce fractions as high as a few per cent for O VI and N VI, while the bulk of the metals reside in the ionization stages IV and V.

## 5.2 I-front encounters the minihalo: weak, R-type phase inside minihalo

As the weak, R-type I-front propagates towards the minihalo, it encounters a steeply rising density, first the infall region and then the virialized region of the minihalo, itself, and its velocity drops precipitously. Figure 11 shows the evolution of the I-front position  $x_I$  (upper panel), its velocity  $v_I$  (middle panel) and the mass fraction  $M/M_{\text{init}}$  of the gas initially within the original hydrostatic sphere (bottom panel) which remains neutral over time in the BB 5e4 case. The initial speed of the I-front as it enters the box is about  $10,000 \text{ km s}^{-1}$ , dropping to  $\sim 1000 \text{ km s}^{-1}$  by the time the front crosses the virial radius of the halo. As a result, the I-front is initially a weak, R-type front even after it enters the minihalo. It takes about 5 Myr for the front to slow to the R-critical front speed  $v_R \cong 2c_{s,2} \approx 20 \text{ km s}^{-1}$  (where the isothermal, post-front sound speed  $c_{s,2} \cong 11 \text{ km s}^{-1}$ ) (marked on the plot by an arrow) after which a compressive shock must form to lead the I-front and further decelerate it, so as to transform it to a D-type front. On the top panel, we have indicated (by another arrow) the position of the inverse Strömgren surface at zero impact parameter, as calculated in § 2.3. The two arrows almost coincide, confirming our expectations of approximate correspondence between the ISL (in the static analytical calculation) and the surface on which the I-front is R-critical, close to the moment of conversion of the I-front to D-type (also indicated in Fig. 2). This correspondence is not perfect, however, due to the significant approximations made in the ISL calculation. For example, due to the centrally-concentrated halo density profile the I-front transition to D-type occurs in fact at different times for each impact parameter, leading to a continuously evolving I-front shape different from the shapes shown in Figure 3.

Figures 12 and 13 show the time-slice at 0.2 Myr, shortly before the weak, R-type I-front enters the minihalo. The instantaneous position of the I-front is indicated on the top panel which shows the contours of pressure. The I-front moves faster further away from the halo due to the lower density in the infall profile and has already significantly slowed down closer to the axis. The harder photons clearly penetrate significantly deeper in the QSO and BB 1e5 cases and the halo shadow is already clearly outlined at that time by the pressure contours, even though the front itself has not passed the halo yet. These same hard photons also start to heat the halo on the source side, while deeper into the halo and in the shadow region behind it virtually no photons can penetrate due to the extremely high optical depth,  $\tau \sim 10^4$  (bottom panels). While the shadow is mostly neutral in all cases, the QSO case produces a  $10^{-4}$  fraction of He II and He III there.

In Figures 14-17 we show the structure of the flow at  $t = 2.5$  Myr, when the I-front is inside the minihalo but still a weak, R-type front, before much hydrodynamical back-reaction has begun. Figure 14 and 15 show that the gas which was initially infalling on the source side next to the halo is already reversing its velocity, however, and starting to form a shock which will sweep the IGM outward. On the

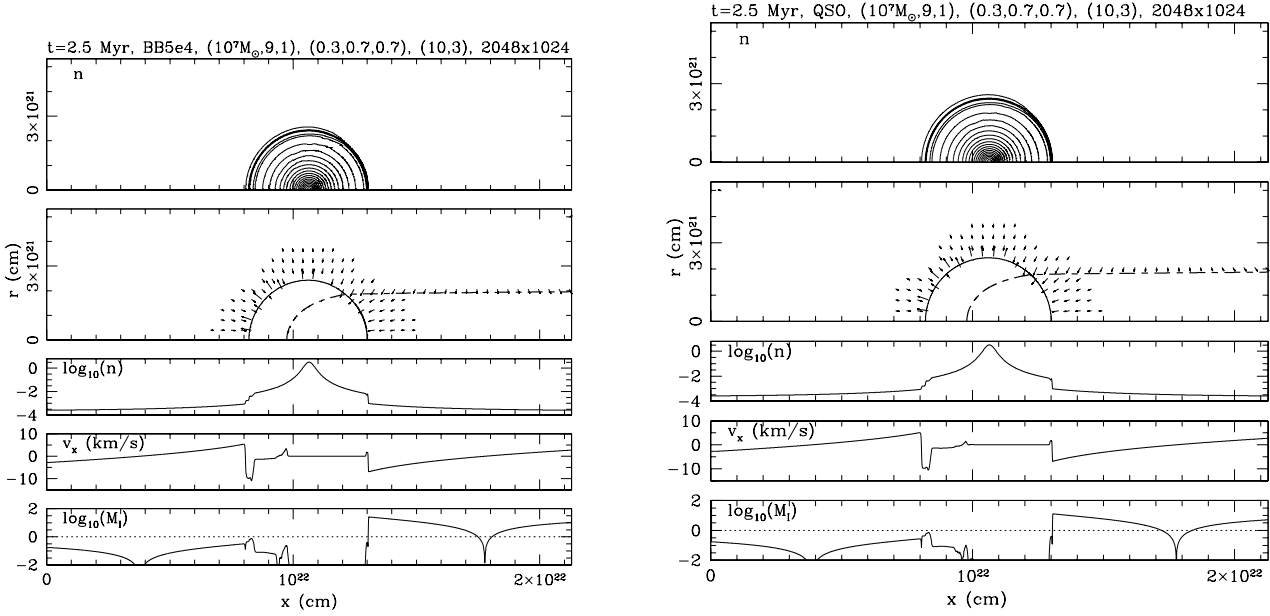


**Figure 14.** Weak, R-type phase of I-front inside the minihalo. Same as Figure 5, but for later time-slice,  $t = 2.5$  Myr after I-front enters the box: (a) (left) BB 5e4 case and (b) (right) QSO case. A velocity arrow of length equal to the spacing between arrows has velocity  $10 \text{ km s}^{-1}$ ; minimum velocities plotted are  $3 \text{ km s}^{-1}$ . Solid line shows current extent of gas initially inside minihalo at  $z = 9$ . Dashed line indicates the current position of the I-front (50% H-ionization contour).

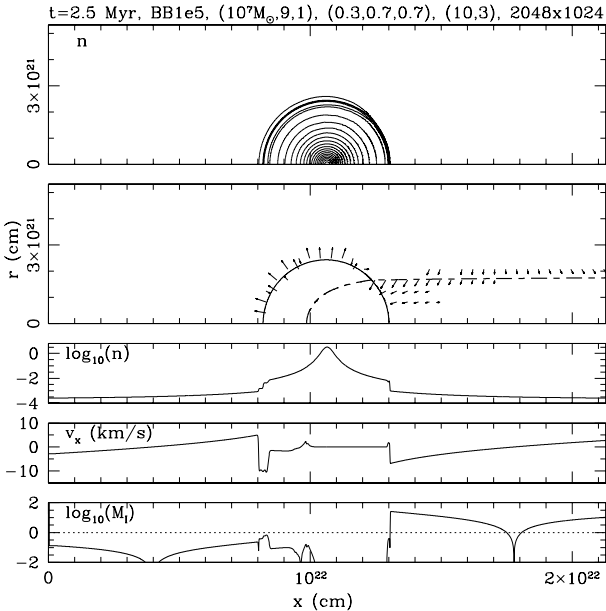


**Figure 15.** Same as in Figure 14, but for BB 1e5 case.

other hand, on the shadow side of the halo, the gas infall continues uninterrupted. Also evident is some squeezing of the gas in the shadow due to the much higher pressure of

the ionized gas outside it after the passage of the fast R-type I-front there.

### 5.3 I-front trapping: R-critical phase and the transition from R-type to D-type

The I-front finally slows to become an R-critical front by 5 Myr. We show the results for this time-slice for all three source spectra in Figures 18–22. To illustrate clearly that this is the R-critical phase, we focus on the Pop II stellar case BB5e4 in Figure 18 and “zoom in” on the region around the I-front along the  $x$ -axis in Figure 19. All of the important properties of an R-critical I-front are evident in Figure 19. The I-front velocity at this epoch is  $v_I \approx 16 \text{ km s}^{-1}$  which is not far from the estimated R-critical value of  $v_R \approx 20 \text{ km s}^{-1}$ , calculated based upon the immediate post-front temperature of  $T_2 \approx 10,000 \text{ K}$ , the pre-front  $T_1 = 4,000 \text{ K}$  (i.e. the neutral side is undisturbed minihalo gas at this virial  $T$ ),  $\mu_1 = 1.11$  (i.e. 90% neutral), and  $\mu_2 = 0.63$  (i.e. 90% ionized H), which yield the post-front and pre-front isothermal sound speeds  $c_{s,I,2} = 11 \text{ km s}^{-1}$  and  $c_{s,I,1} = 5.3 \text{ km s}^{-1}$ , respectively. The numerical results show the predicted jump in density by a factor of close to two across the R-critical I-front, required by the I-front jump conditions. In addition, in the lab frame in which the neutral minihalo gas on the pre-front side is at rest (i.e. the frame in which we have plotted velocity and isothermal Mach number in Figures 18 and 19), the ionized gas just

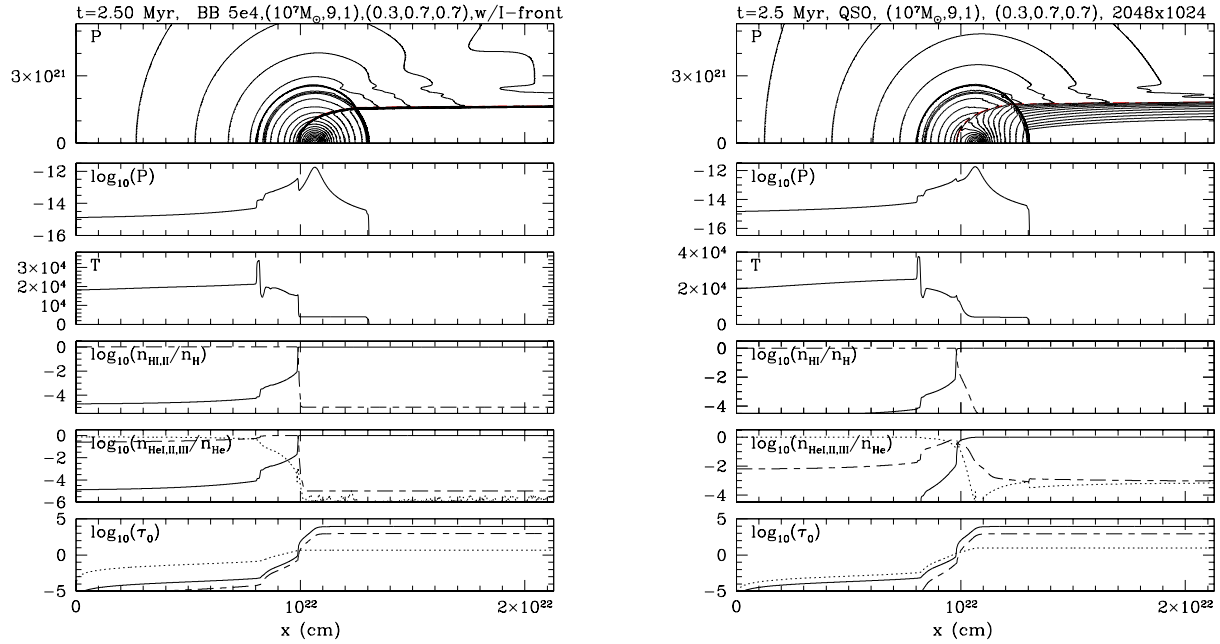


**Figure 16.** Weak, R-type phase of I-front inside the minihalo. Same as Figure 12, but for  $t = 2.5$  Myr.

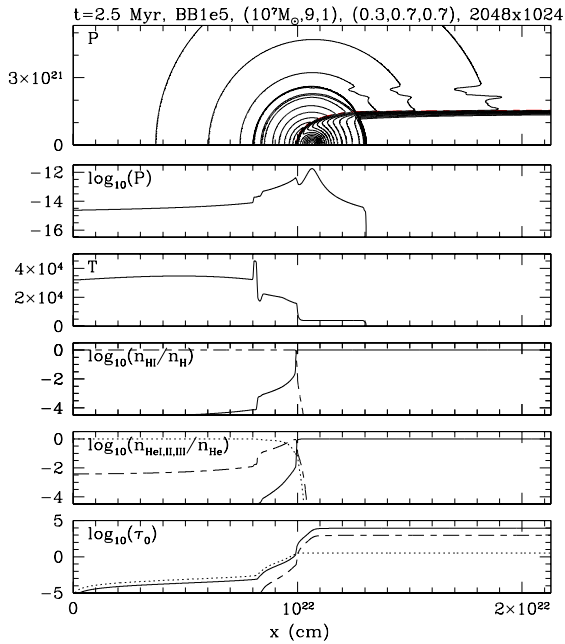


**Figure 17.** Same as in Figure 16, but for BB 1e5 case.

behind the front should be moving toward the neutral side at the isothermal sound speed of the ionized post-front gas, or about  $11 \text{ km s}^{-1}$ , which our plots confirm (i.e. note that the isothermal Mach number  $M_I = 1$  at that point in lower panel of Fig. 19). It is interesting to note that, while the gas on the ionized side of the I-front is generally optically thin

during most of the evolution, the optical depth is not negligible at  $t = 5$  Myr. According to Figure 19, the H optical depth across the ionized, post-front layer is of order a few, so the speed of the I-front is lower than would be calculated using the unattenuated flux in the I-front continuity jump condition.

This R-critical phase is the beginning of the transition to D-type, which should occur shortly, thereafter, when a shock wave forms to compress the gas ahead of the front, to enable the front velocity to drop to the D-crit value. In this case, using the sound speeds at 5 Myr reported above, the D-critical velocity is  $v_D \approx c_{s,I,1}^2 / (2c_{s,I,2}) \cong 1.35 \text{ km s}^{-1} \ll v_R$ . As we can see from the plot of  $v_I$  in Figure 11, however, the transition from R-type to D-type is quite extended in time, lasting 10's of Myr. During that same time, the I-front advances into denser and denser neutral minihalo gas, which also slows the front quite apart from any dynamical compression which might lead the front. In the meantime, from the R-critical phase onward, the hydrodynamical response to the I-front becomes more and more dramatic.

#### 5.4 The structure of the photoevaporative flow during the D-type I-front phase

When the I-front slows to become a D-type front, the hydrodynamical response of the gas catches up with it and leads to the complete photoevaporation of the minihalo. This photoevaporative flow exhibits many generic features which are independent of the spectrum of the ionizing source. The side facing the source expels a supersonic wind backwards towards the source. There is a wind shock which thermalizes

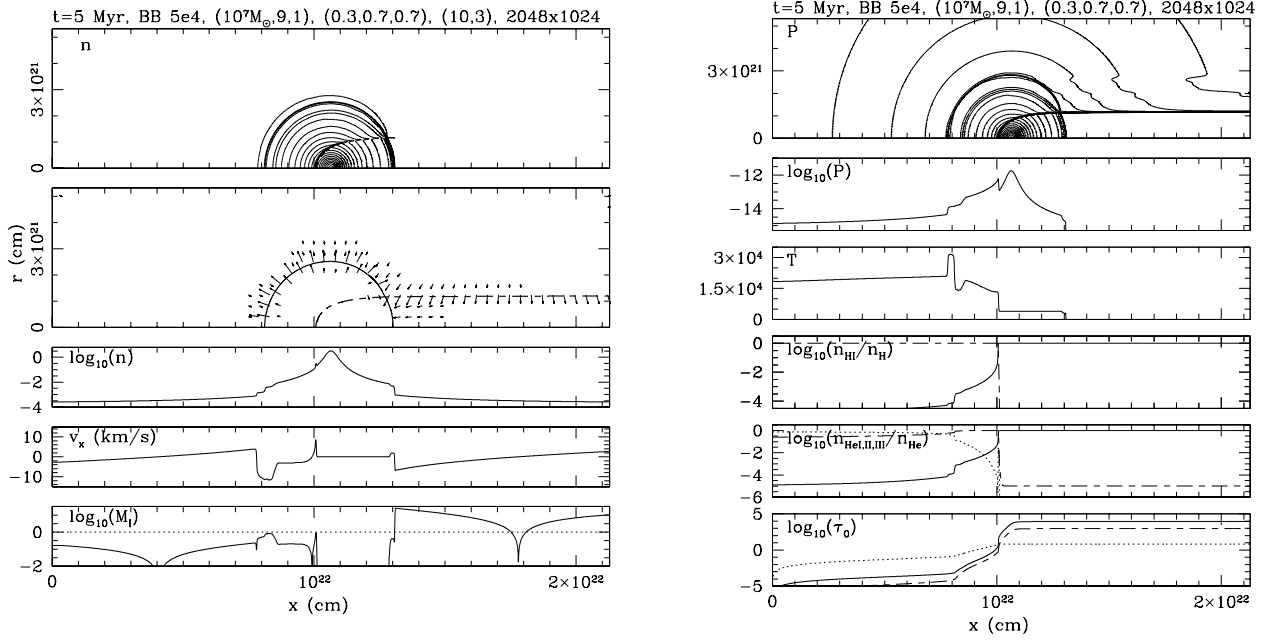


**Figure 18.** R-critical phase of I-front just before transition from R-type to D-type. (a) (left) Panels show same quantities as in Fig. 14, but for  $t = 5$  Myr and BB5e4 case; (b) (right) Same quantities as in Fig. 12, but for the  $t = 5$  Myr and BB5e4 case.

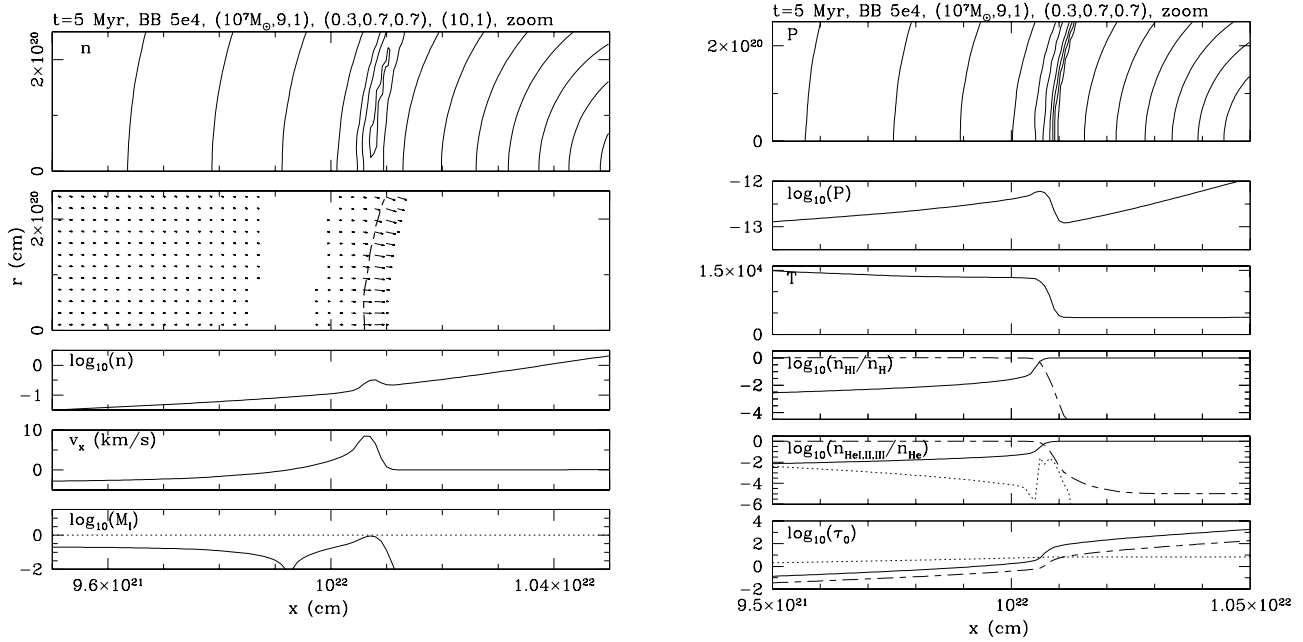


**Figure 19.** Same as Fig. 18, but “zoom-in” to enlarge the view of R-critical I-front along the  $x$ -axis.

this wind outflow and separates the unshocked supersonic wind close to the ionized side of the I-front from the shell of shocked wind further away from the I-front on this side. The shocked wind gas acts as a piston which sweeps up the photoionized IGM outside the minihalo and drives a shock into

the IGM, reversing its infall velocity. The wind grows more isotropic with time as the remaining neutral halo material is photoevaporated. Since this gas was initially bound to a dark halo with  $\sigma_V < 10 \text{ km s}^{-1}$ , photoevaporation proceeds unimpeded by gravity. In Figures 22–26, we show the struc-

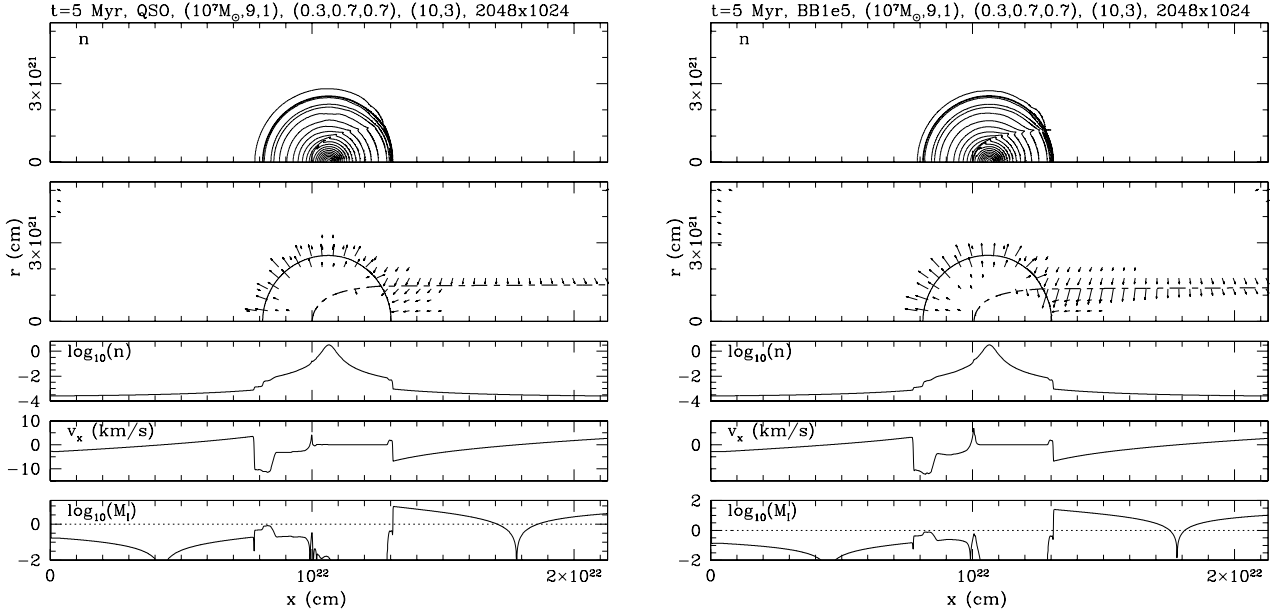


**Figure 20.** R-critical phase of I-front just before transition from R-type to D-type. Panels show same quantities as in Fig. 14, but for 5 Myr: (a) (left) QSO case; (b) BB1e5 case.

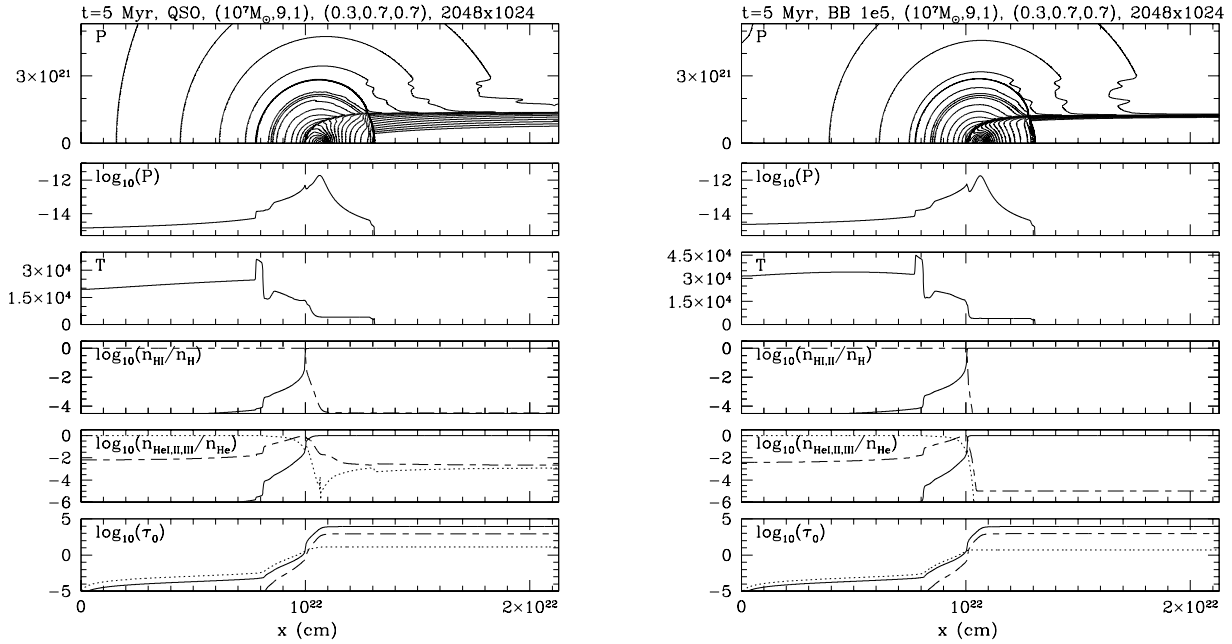


**Figure 21.** R-critical phase of I-front just before transition from R-type to D-type. Panels show same quantities as in Fig. 12, except for  $t = 5$  Myr: (a) (left) QSO case; (b) BB1e5 case.

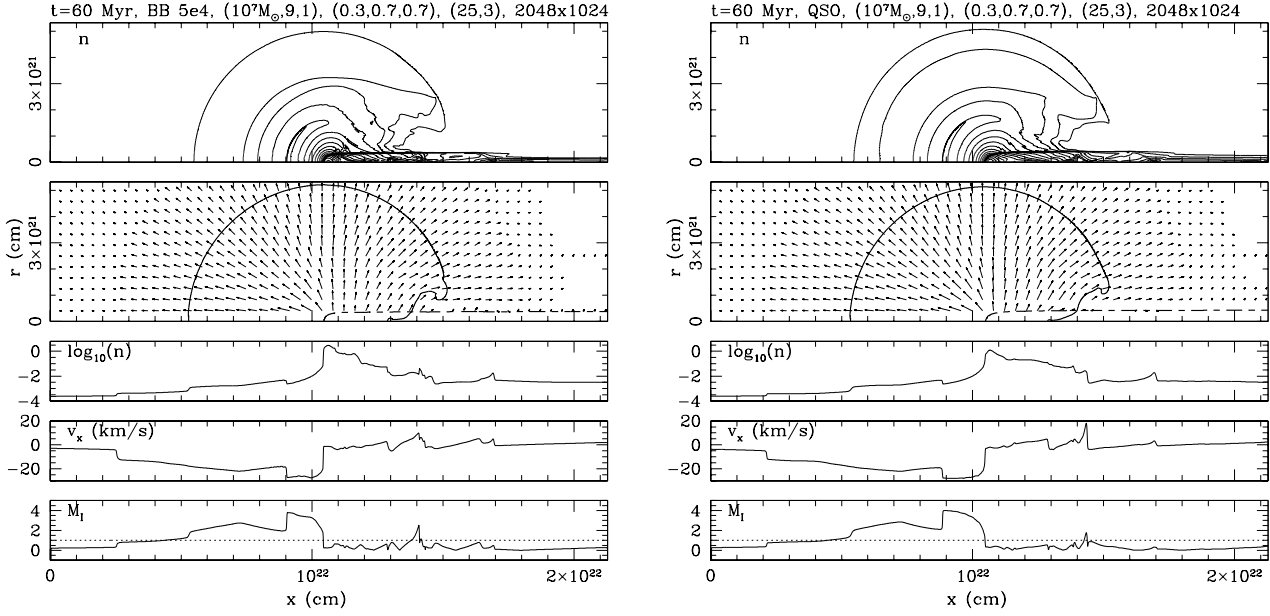


**Figure 22.** D-type phase of I-front: Photoevaporative Flow 60 Myr after I-front overtakes the minihalo: (a) (left) BB 5e4 case and (b) (right) QSO case. Same quantities plotted as in Fig. 14, except  $t = 60$  Myr.

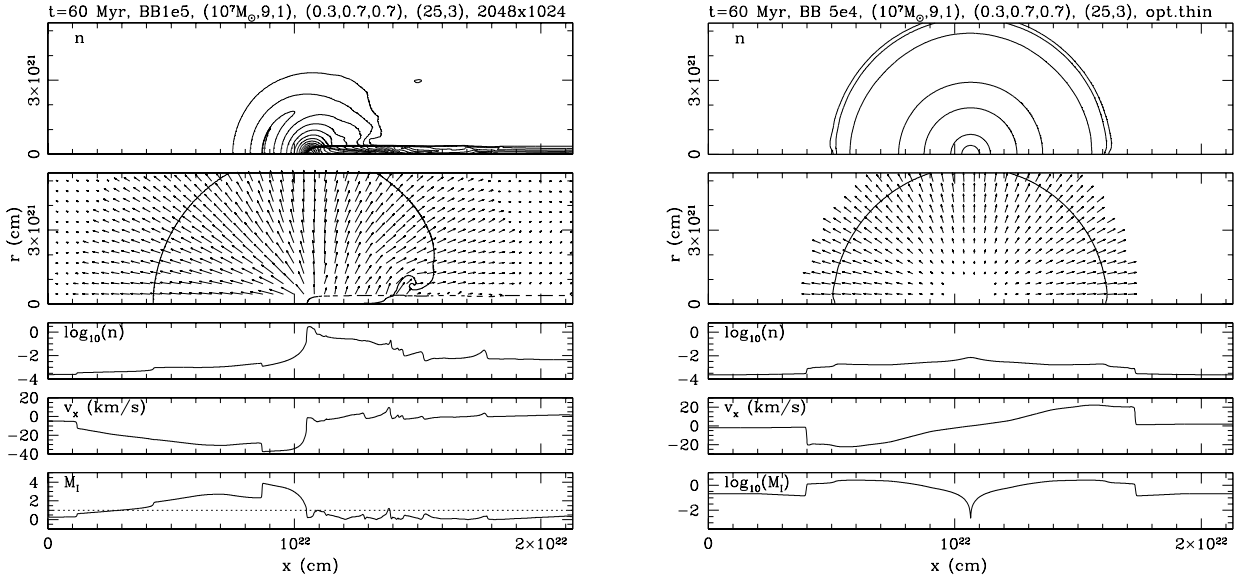


**Figure 23.** (a) (left) Same as Figure 22, but for BB 1e5 case. (b) (right) Same time-slice as Figure 22, but for optically-thin BB 5e4 case.

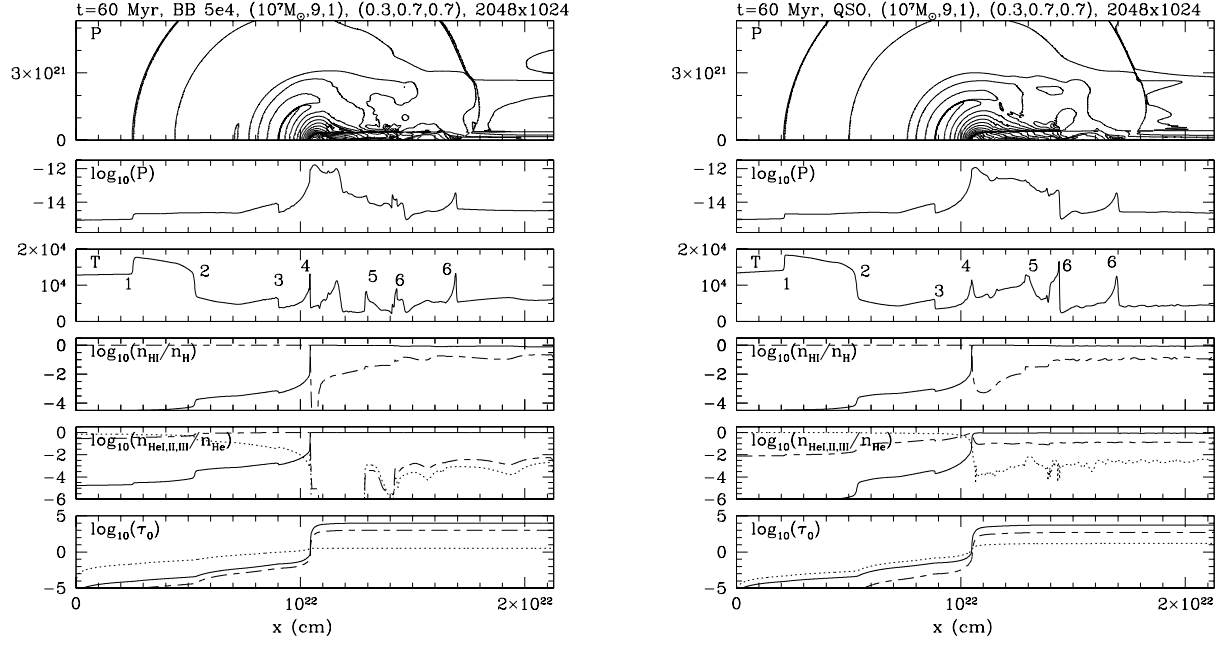


**Figure 24.** D-type phase of I-front: Photoevaporative Flow 60 Myr after I-front overtakes the minihalo: (a) (left) BB 5e4 case and (b) (right) QSO case. Panels show the same quantities as in Figure 12. Key features of the flow are indicated by the numbers which label them on the temperature plots: 1 = IGM shock; 2 = contact discontinuity which separates shocked halo wind (between 2 and 3) from swept-up IGM (between 1 and 2); 3 = wind shock; between 3 and 4 = supersonic wind; 4 = I-front; 5 = boundary of gas initially inside minihalo at  $z = 9$ ; 6 = shock in shadow region caused by compression of shadow gas by shock-heated gas outside shadow.

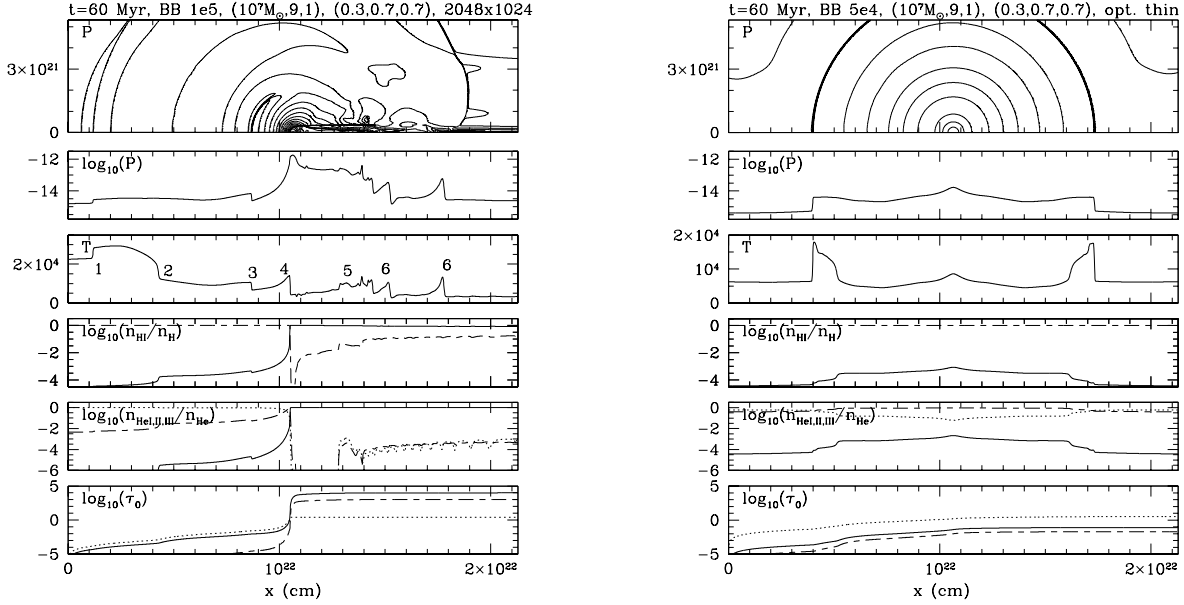


**Figure 25.** (a) (left) Same as Figure 24, but for BB 1e5 case. (b) (right) Same as Figure 24, but for optically-thin BB 5e4 case.

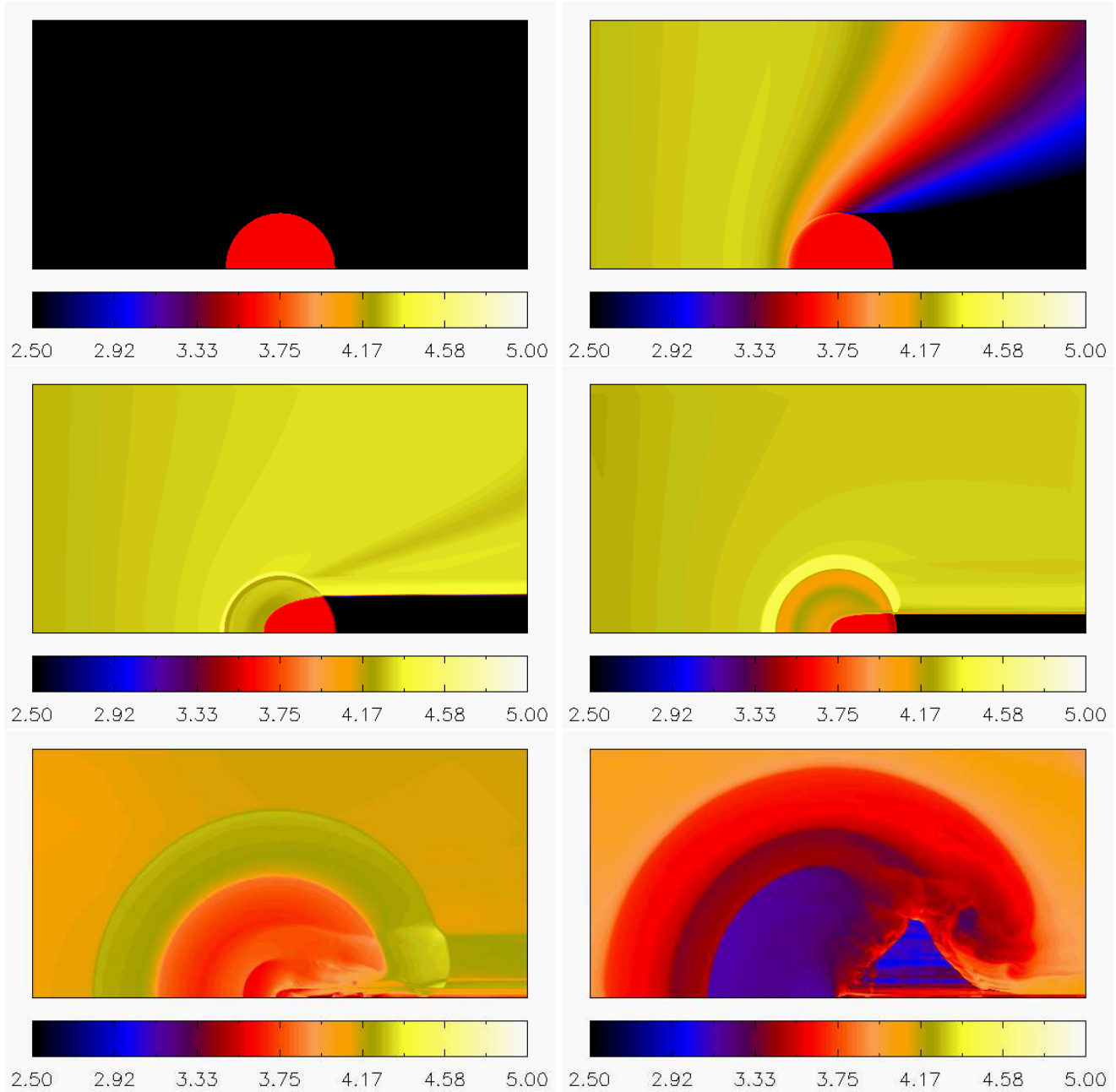


**Figure 26.** Snapshots of the temperature at times  $t = 0$  (top left), 0.2 (top right), 2.5 (middle left), 10 (middle right), 60 (bottom left), and 150 (bottom right) Myr in the BB5e4 case. Shaded isocontours are logarithmic in temperature. Colors indicate the values of  $\log_{10}(T)$ , as labelled on the color bar.

ture of the flow at a time 60 Myr after the global I-front first overtakes the minihalo. In Figure 22 and the left panels of Figure 23 we show the density contours of the gas, the current position of the ionization front, the velocity field, the current extent of the original halo material, and profiles of gas number density, velocity and Mach number along the  $x$ -axis. In all three cases, the typical speed of the photoionized outflow is supersonic and roughly proportional to the sound

speed of the ionized gas. Hence, the outflow is fastest in the BB 1e5 case, due to the higher photoionization temperature reached in this case.

For comparison, we have also performed a simulation of this problem in the optically-thin approximation (i.e. zero optical depth), to demonstrate the inadequacy of such an approximation. In Figure 23 (right panels), we plot the results for this optically-thin photoevaporation simula-



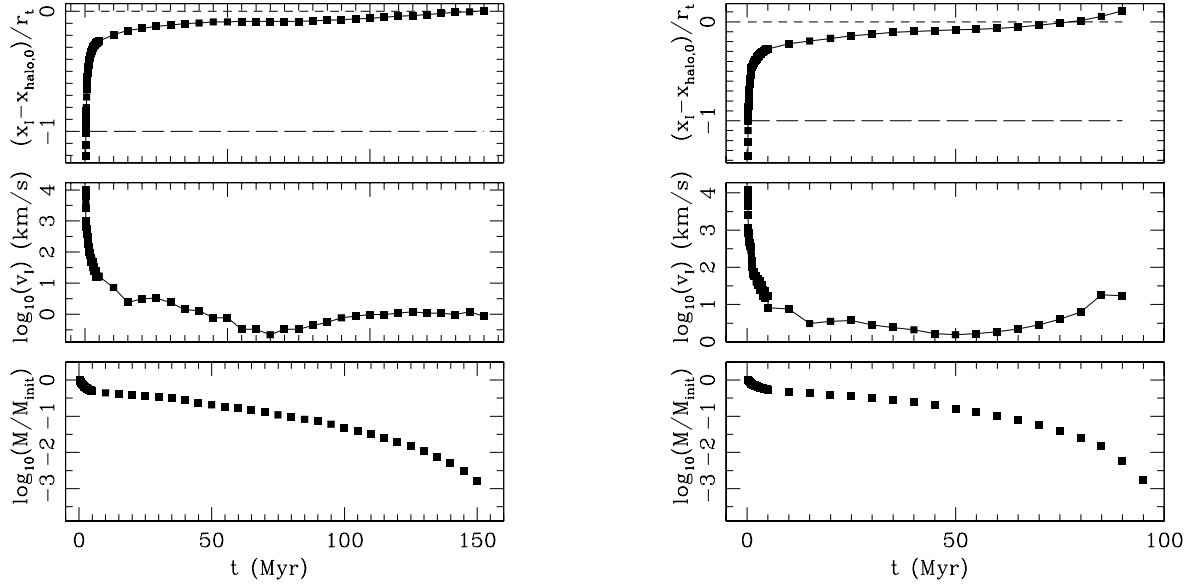


**Figure 27.** Evolution of I-front position and velocity and of the neutral gas content of photoevaporating minihalo: (a) (left) BB 5e4 case and (b) (right) QSO case. (upper panels) Position  $x_I$  (in units of the minihalo radius  $r_t$  at  $t = 0$ ) and (middle panels) velocity  $v_I$  of an ionization front propagating toward and through the minihalo. The positions of the boundary (long-dashed line) and centre of the halo (short-dashed line) are also indicated. (lower panels) Fraction of mass  $M_{\text{init}}$ , the mass which is initially inside the minihalo when the intergalactic I-front overtakes it, which remains neutral versus time  $t$ .

tion for exactly the same halo and source parameters as the BB 5e4 spectrum case shown in Figure 22 (left panels), for the same time-slice. In the optically-thin case, the halo is suddenly and uniformly ionized and photoheated to  $T \sim 20,000 - 35,000$  K, well above its virial temperature. Thereafter, the large pressure gradient causes the gas to expand isotropically in all directions unimpeded by gravity, producing a completely different flow structure.

For the more realistic simulations which included radiative transfer, Figures 24 and 25 show the pressure contours, and the profiles along the symmetry axis for pressure, temperature, H I-II fractions, He I-III fractions, and optical depths at the ionization thresholds of H I, He I, and He II, for the photoevaporative flow 60 Myrs after the global I-front first overtakes the minihalo. Key features of the flow are indicated by the labels on the temperature panels. For comparison, we also show the very different results for these quantities in the optically-thin simulations (Figure 25, right panels).

### 5.5 Evolution of the temperature structure

The different stages of the photoevaporation process are illustrated in Figure 26 by shaded isocontours of temperature for a sequence of time-slices of the BB 5e4 case. The panels show: (a) (time  $t = 0$  Myr), the initial condition of the isothermal, virialized halo surrounded by a cold, infalling, IGM; (b) ( $t = 0.2$  Myr), the fast, R-type I-front sweeping

through the computational box is just about to encounter the minihalo along the  $x$ -axis, and is starting to photoheat the halo on the source side; (c) ( $t = 2.5$  Myr), when the weak, R-type I-front is inside the minihalo before it slows to R-critical and begins to transform to D-type, a distinct shadow is apparent behind the neutral portion of the halo, while the rest of the gas is heated to  $T > 10^4$  K, and the photoevaporation process begins; (d) ( $t = 10$  Myr), the R-type to D-type transition phase, when the I-front slowly advances along the axis, the shadow region behind the shielded, neutral minihalo core is reduced, and the IGM shock and the shocked wind are clearly visible; (e) ( $t = 60$  Myr), strong D-type phase, when the shadow is being ablated and the remaining gas heated, by shocks reflected off the  $x$ -axis behind the halo. The key features of the flow indicated in Figure 24 are all clearly seen; (f) ( $t = t_{\text{ev}} = 150$  Myr, the evaporation time), when the gas is almost completely evaporated from the halo and resides in a much larger, low-density region which is cooling adiabatically as it expands, leaving behind a dark-matter halo almost completely devoid of gas. Movies of these simulation results, including the time evolution of additional quantities like pressure, density, H I and He I fractions, and the results for the cases with different source spectra are available at <http://galileo.as.utexas.edu>.

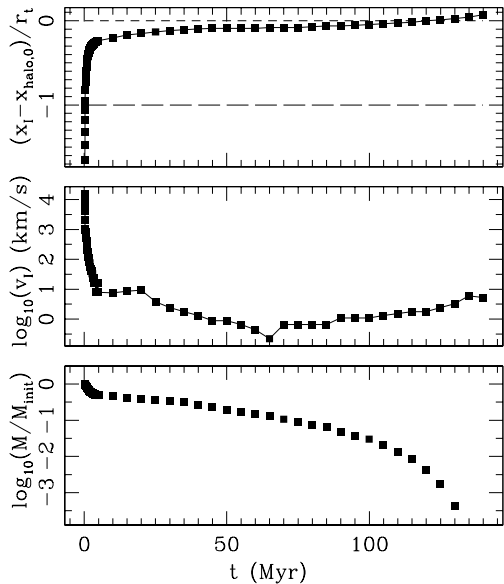


**Figure 28.** Same as Figure 27, but for BB 1e5 case.

### 5.6 I-front evolution

The evolution of the position  $x_I$  and velocity  $v_I$  of the I-front, and of the remaining neutral mass fraction  $M/M_{\text{init}}$  are shown for all three source spectra cases in Figures 27 and 28, for comparison. The weak, R-type I-front slows down to the R-critical velocity about 5 Myr after it reaches the minihalo, after which a shock must form ahead of the I-front to compress the gas and slow it down to D-critical velocity or below, as discussed in detail in § 5.2. The further evolution is slower and more gradual. Eventually, the I-front speed drops below the D-critical front speed  $v_D \approx 1 \text{ km s}^{-1}$ . For the rest of the evaporation process, the velocity of the I-front is  $\lesssim 1 \text{ km s}^{-1}$ , i.e. sub-critical. At 60 Myr, for example, the I-front velocity has dropped to about  $v_I \sim 0.3 \text{ km s}^{-1}$ , while the D-critical velocity is still  $v_I \approx 1 \text{ km s}^{-1}$ . This behaviour is different from the usual approximation made in analytical calculations of photoevaporation, in which the I-front is assumed to be D-critical.

What kind of D-type front is it during the D-type phase? Weak, D-type fronts move subsonically with respect to both the neutral and ionized gas. Strong D-type fronts move subsonically into the neutral gas but supersonically with respect to the ionized gas. In the lab frame (i.e. rest frame of the neutral gas before ionization), as the D-type front advances into the neutral side (i.e. away from the source), the ionized gas behind it always moves *toward* the source (i.e. opposite to direction of I-front). This ionized gas motion can be either subsonic (for weak fronts), or almost sonic (for D-critical fronts), but it is supersonic only for *strong* D-type fronts. If we apply this description to our 60 Myr time-slice for the BB5e4 case and look both at the I-

front velocity evolution plot in Figure 27 and the cuts along the  $x$ -axis in Figure 22, we see that the I-front is subcritical at that point. From the Mach number plot at points just behind the I-front on the immediate post-front (ionized) side, the lab frame velocity is supersonic toward the source, which indicates that the front is a strong, D-type. This is consistent with the density cut along the  $x$ -axis which shows that density *drops* by a very large amount from the neutral to the ionized side, as it should for both weak and strong, D-type fronts, but the strong type has an even bigger drop in density, as required to explain the numerical results. In short, the I-front at 60 Myr is a subcritical, strong, D-type.

### 5.7 Evaporation times

The neutral mass fraction of the original minihalo gas quickly drops to  $\sim 60$  per cent during the initial slowing-down phase of the I-front evolution, and subsequently declines much more gradually as the minihalo photoevaporates. We define the photoevaporation time  $t_{\text{ev}}$  as the time when only 0.1 per cent of the mass remains neutral (i.e. when  $M/M_{\text{init}} = 10^{-3}$ ). We see from Figures 27 and 28 that, once the neutral mass fraction reaches  $\sim 1$  per cent, it drops fairly precipitously, indicating that the value of  $t_{\text{ev}}$  is not sensitive to our particular choice of the final value for  $M/M_{\text{init}}$  used to define this evaporation time. We obtain  $t_{\text{ev}} \approx 150, 125$  and  $100$  Myrs for the BB 5e4, BB 1e5 and QSO cases, respectively. Compared to the BB 5e4 case, the evaporation time in the BB 1e5 case is shorter due to the higher outflow velocity in this case (see Fig. 23), caused by the higher temperature in the photoionized region. In the QSO case, on the other hand, the outflow velocity is similar to the one in the BB 5e4 case, but the photoevaporation process in this case is accelerated by the significant pre-heating due to the hard photons present in this spectrum, which ultimately leads to an even shorter  $t_{\text{ev}}$ . These values of  $t_{\text{ev}}$  are all within a factor of two of the sound crossing time for an ionized gas sphere of the same diameter as our minihalo reported in §2.4. However, we caution that this result is not a proof that  $t_{\text{sc}}$  is a good estimator of  $t_{\text{ev}}$ . In fact, results for a wide range of halo and source parameters which we shall present in a companion paper demonstrate that  $t_{\text{ev}}$  departs significantly from  $t_{\text{sc}}$ , in general.

### 5.8 Ionizing photon consumption

#### 5.8.1 Minihalo effective cross-section

The gradual decay of the opaque cross section of the minihalo as seen by the source [as defined in eq. (27)] is illustrated by Figure 29 (left panels) for photons at the ionization thresholds of H I, He I, and He II. For the BB5e4 case, the cross section at the H I threshold drops to 10% of its original value after  $0.4t_{\text{ev}} = 60$  Myr, while the cross section at the He I threshold drops somewhat faster. The cross section of the minihalo at the He II threshold, however, initially rises as the partially ionized gas expands, and only later, around

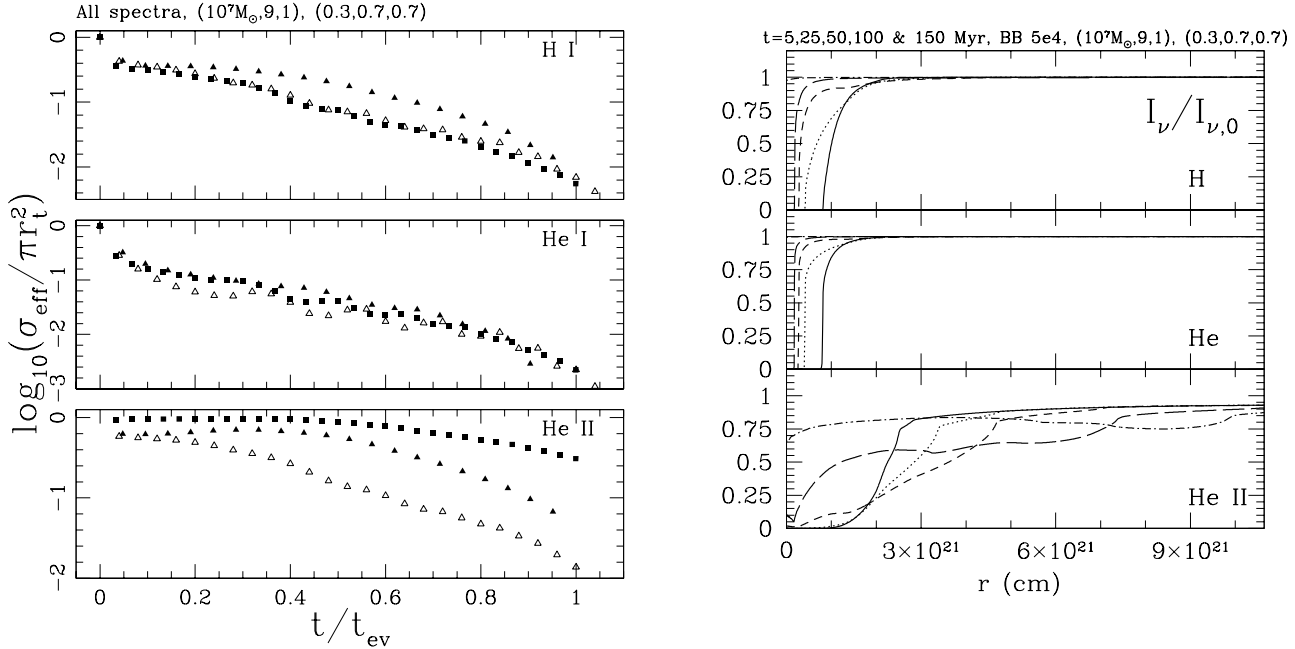


**Figure 29.** (a) (left) Fraction of minihalo initial geometric cross section  $\pi r_t^2$  ( $r_t = 0.76$  kpc) which is opaque to source photons that can ionize H I (top panel), He I (middle panel), or He II (bottom panel) versus time (in units of  $t_{\text{ev}}$ ), for the BB 5e4 (filled squares), QSO (filled triangles) and BB 1e5 (open triangles) cases. ( $t_{\text{ev}} = 150, 100$ , and  $125$  Myr, respectively). (b) (right) Transmitted flux  $I_\nu/I_{\nu,0}$  at the ionization thresholds of H (top), He I (middle), and He II (bottom) vs. impact parameter (or radius in axisymmetry)  $r$  at times  $t = 5$  (solid), 25 (dotted), 50 (short-dash), 100 (long-dash), and 150 (dot-dash) Myr for the BB 5e4 case.

$0.4t_{\text{ev}} = 60$  Myr, does it start to decline slowly, as He II starts to become ionized to He III. The evolution of the H I effective cross-section is similar for the two stellar spectra, but decreases somewhat more slowly in the QSO case, while the evolution of the He II cross-section is similar for all three spectra. Finally, the evolution of the He I cross section is markedly different in all three cases, due to the different photon energy distribution of the three spectra.

In Figure 29, we show the transmitted fluxes at the ionization thresholds of H I, He I, and He II vs. impact parameter  $r$  at times  $t = 5, 25, 50, 100$ , and  $150$  Myr for the BB 5e4 case. We see that the simulation box is optically-thin to the photons with energies below the He II ionization threshold along most lines of sight along the  $x$ -direction outside the minihalo; only the minihalo is significantly opaque, once the global I-front has swept past the minihalo. The minihalo’s cross-section declines quickly with time once the I-front enters it and is somewhat smaller for He I ionizing photons than for H I ionizing photons. The simulation box is never completely optically-thin to He II ionizing photons and has rather complex time behaviour as the wind expands and more He II is photoionized to He III.

### 5.8.2 Number of ionizing photons per atom consumed during photoevaporation

Based on our simulation data, we have calculated the number of ionizing photons per atom,  $\xi$ , required to evapo-

rate a minihalo both by using the effective cross-section method of equation (29) and by counting the total number of recombinations [as in eq. (30)]. Using the first method, we obtain  $\xi = (4.51, 5.41, 3.43)$  in the BB 5e4, QSO, and BB 1e5 cases, respectively, while the second method yields  $\xi = (5.1, 5.0, 3.3)$ . Since the two methods give similar results, we can, henceforth, rely upon either one. For the “efficiency” factor  $f$  in equation (32) (assuming  $T_4 = 1$ ), these results imply  $f = (0.029, 0.034, 0.022)$  and  $f = (0.032, 0.032, 0.021)$ , respectively.

In the optically-thin approximation case, the effective cross-section is, by definition, zero at all times, and thus only the second method for calculation of  $\xi$  is applicable. By contrast with our results which took proper account of the optical depth in bound-free opacity, for which  $f \ll 1$ , our optically-thin results for  $\xi$  by the second approach yield  $f \approx 1$  [consistent with the result obtained in this optically-thin approximation by Haiman, Abel & Madau (2001)]. This enormous overestimate of  $\xi$  by the optically-thin approximation indicates that the optically-thin approximation used by previous authors is completely inadequate for determining  $\xi$ .

The reason for this significant discrepancy is easily understood if we consider where and when most of the recombinations take place. In Figure 30, we show the evolution of  $\xi$  for our illustrative simulations. During the initial R-type phase, the I-front deceleration phase, a significant fraction of the mass ( $\sim 40\%$  in our sample simulations) becomes

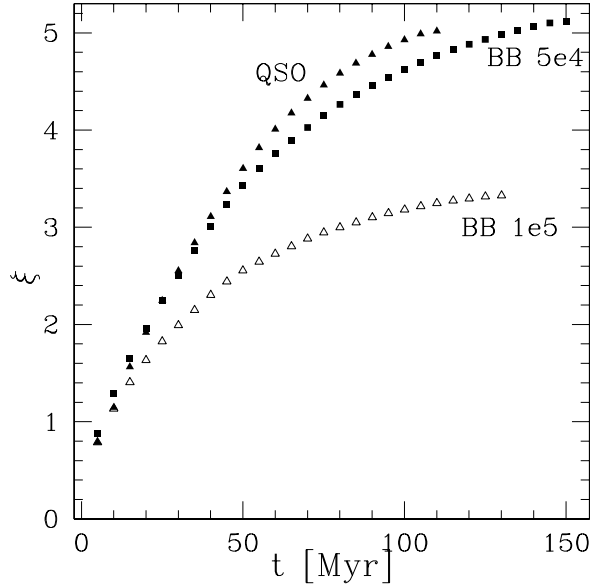


**Figure 30.** Evolution of the consumption of ionizing photons as given by equation (30) for all three spectra, as labelled.

ionized almost instantly, just as does the entire minihalo in the optically-thin approximation. This gas is in the halo outskirts, however, where the density is low and that density drops even further as the gas expands in the evaporative outflow, into the IGM, making recombination in this gas inefficient within 10 – 20 Myr. Most of the minihalo gas is initially shielded, however, and remains neutral for a much longer time. From this point on, the additional ionization of gas occurs only where the photoevaporation process is removing it by expelling it in a supersonic wind. For this gas, the density becomes too low too soon for significant recombinations to occur there. Therefore, during most of the evolution, the bulk of the recombinations occur in a thin dense layer in the immediate vicinity of the I-front. Each gas atom spends only a short time in this layer, however, as it rushes supersonically away from the neutral region into the low-density expanding wind, hence experiencing many fewer recombinations than the optically-thin approximation would predict.

As Figure 30 shows,  $\xi$  increases gradually throughout the evaporation time, and there are noticeable differences among the three cases. For the hard QSO spectrum, the transition layer is thicker and penetrates deeper into the denser and colder parts of the halo, thus increasing the number of recombinations per atom per evaporation time. However, this same pre-heating effect shortens the evaporation time in this case, ultimately leading to a rough cancellation of the two effects and the same total  $\xi$  as in the BB 5e4 case. The BB 1e5 spectrum is not as hard as in the QSO case, which decreases the number of recombinations in the I-front layer. The evaporation time in this case is also shorter than in the BB 5e4 case, due to a higher photoionization

temperature and thus to faster outflow speed. Additionally, the higher temperatures in the wind for the BB 1e5 case ( $\sim 10^4$  K, as opposed to  $\sim 5000$  K in the other two cases, see Figs. 24 and 25) also leads to lower rates of recombination in the wind and again lower  $\xi$ . Thus, overall, the Pop. III sources appear significantly more efficient than Pop. II or QSO sources in terms of the total number of ionizing photons needed to complete the photoevaporation process.

In principle, the optically-thin approximation might become correct in the limit of  $\chi_S \gg \chi_{S,\text{crit}}$  (see § 2.3), in which case the I-front is not trapped, the minihalo is ionized almost instantly compared to the evaporation time, and the radiative transfer effects are less significant. However, for most minihalos this is not a relevant limit, since it requires excessively high ionizing flux of  $F_0 \gtrsim 100 - 1000$  (depending on the halo mass and redshift of collapse) (see § 2.2).

## 5.9 Observational diagnostics

### 5.9.1 Absorption lines

Some observational signatures of the photoevaporation process are shown in Figures 31–34. In Figures 31 and 32, we show histograms of the column densities of H I, He I and II, and C IV for minihalo gas at different radial velocities as seen along the symmetry axis at different times, to illustrate the kind of absorption lines which a photoevaporating minihalo might produce. At early times, the minihalo gas resembles a weak damped Ly $\alpha$  (“DLA”) absorber with small velocity width ( $\gtrsim 10 \text{ km s}^{-1}$ ) and  $N_{\text{HI}} \gtrsim 10^{20} \text{ cm}^{-2}$ , with a Ly $\alpha$ -Forest (“LF”)-like red wing (velocity width  $\gtrsim 10 \text{ km s}^{-1}$ ) with  $N_{\text{HI}} \sim 10^{15} \text{ cm}^{-2}$  on the side moving toward the source. As photoevaporation proceeds, this red wing increases in H I column density to  $N_{\text{HI}} \sim 10^{17} \text{ cm}^{-2}$ . The He I profile mimics that of H I but with  $N_{\text{HeI}}/N_{\text{HI}} \sim [\text{He}]/[\text{H}]$ , and there is a weak C IV feature with  $N_{\text{CIV}} \sim 10^{10} (10^{12} \eta) \text{ cm}^{-2}$  for the BB 5e4 (QSO, BB 1e5) cases, respectively, displaced in this same asymmetric way to the red side of the velocity of peak H I column density, where  $\eta \equiv [\text{C}]/[\text{C}]_{\odot} \times 10^3$ . For He II at early times, the QSO and BB 5e4 cases have  $N_{\text{HeII}} \approx 10^{18} \text{ cm}^{-2}$  at velocities close to those of the H I peak, and a red wing shifted by  $\sim 10 \text{ km/sec}$  to the red, with  $N_{\text{HeII}} \sim 10^{17} \text{ cm}^{-2}$  which increases over time to  $10^{18} \text{ cm}^{-2}$ . He II qualitatively follows the H I and He I profiles in these cases. For the BB 1e5 case, however,  $N_{\text{HeII}} \approx 10^{18} \text{ cm}^{-2}$  in the H I peak, at early times, decreasing to  $N_{\text{HeII}} \approx 10^{17} \text{ cm}^{-2}$  over time, with a red wing with  $N_{\text{HeII}} \approx 10^{17} \text{ cm}^{-2}$  which increases to  $N_{\text{HeII}} \approx 10^{18} \text{ cm}^{-2}$ . In this case, the He II profile notably diverges from the H I profile. After about an evaporation time, both H I and He I column densities decrease to LF-like values of  $10^{13} - 10^{14} \text{ cm}^{-2}$ , and shortly thereafter the minihalo is completely evaporated. Finally, the C IV column density is greatest in the red wing formed by the evaporative wind, except at the earliest times.

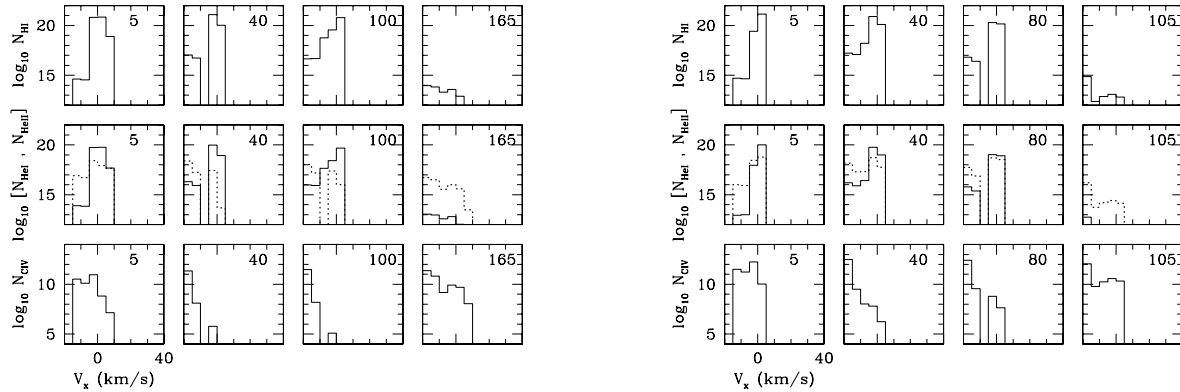


**Figure 31.** Observational diagnostics I. Absorption lines. Minihalo column densities ( $\text{cm}^{-2}$ ) along symmetry axis for gas at different velocities, for photoevaporating minihalo. (a) (left) BB 5e4 case; (b) (right) QSO case. (Top) H I; (Middle) He I (solid) and He II (dotted); (Bottom) C IV (if  $[C]/[C]_{\odot} = \eta \times 10^{-3}$ , then plotted values are  $N_{\text{CIV}}/\eta$ ). Each box labeled with time (in Myr) since arrival of intergalactic I-front.

### 5.9.2 Ionization structure of metals

Figures 33 and 34 show the spatial variation of the relative abundances of C, N, and O ions along the symmetry axis at  $t = 60$  Myrs. While the QSO case shows the presence at 60 Myrs of low as well as high ionization stages of the metals, up to C V, N VI and O VI on the source side of the minihalo and C III on the neutral side, the softer spectrum of the BB 5e4 case yields less highly ionized gas both on the ionized side of the I-front (C III, N III, O III) and the neutral side (C II, N I, O I and II). The BB 1e5 case is intermediate between the other two cases, ionizing carbon up to C V, but ionizing nitrogen and oxygen mostly to N IV and O IV, respectively, with smaller fractions of N V and O V and much smaller, although not negligible fractions of N VI and O VI than in the QSO case. In the optically-thin approximation case in Figure 34 (right panels), similar high ionization stages are reached for the ionized gas exposed to the same photoionizing spectrum as in the results above which took proper account of optical depth, but the low ionization stages of neutral or partially ionized gas are entirely missing. In the optically-thin results, all the gas is ionized instantly, no neutral region of minihalo or shadow exists and the flow expands symmetrically in all directions, which would lead to quite different spectral signatures as compared to the realistic optically-thick cases shown above.

## 6 SUMMARY AND CONCLUSIONS

We have presented the first numerical gas dynamics and radiative transfer simulations of the encounter between an intergalactic I-front and a minihalo during cosmic reionization at high redshift, resulting in the photoevaporation of the minihalo gas. We have studied all stages of the photoevaporation process in detail, starting from the propagation

of the fast, weak, R-type I-front in the low-density IGM, its structure and extent in pressure, temperature and ionization of H, He and a possible trace of metals for different possible source spectra, corresponding to quasars, Pop. III and Pop. II stars. We have demonstrated for the first time the phenomenon of I-front trapping when the global R-type I-front runs into a minihalo along its path and slows down inside the minihalo to an R-critical front, after which the front inside the minihalo transform from an R-type to a D-type front. We have shown that the heated and ionized gas behind the front then expands supersonically into the IGM, sweeping it up and shock-heating it. This process exposes further layers of the minihalo gas to the ionizing radiation from the external source, heating and evaporating them until all the gas is finally expelled from the minihalo. For our illustrative case of a  $10^7 M_{\odot}$  halo, overtaken at  $z = 9$  by an intergalactic I-front created by a source of  $10^{56}$  ionizing photons per second at distance of 1 Mpc (or equivalently, a source of  $10^{52} \text{sec}^{-1}$  at 10 kpc), this process is completed within  $\sim 100 - 150$  Myr, depending on the source spectrum.

The results presented here are fully consistent with our earlier simulations of minihalo photoevaporation, going back to Shapiro, Raga, & Mellema (1997, 1998) and continuing through those in Shapiro & Raga (2000a,b; 2001), and Shapiro (2001), although there are some quantitative differences which result from improvements we have made since then. However, these results differ from those which have appeared in the meantime in the recent literature. As mentioned in §1.3, for example, Barkana & Loeb (1999) considered the photoevaporation of minihalos without gas dynamics and without treating the propagation of the I-front. Their calculations are similar in spirit to (albeit more sophisticated than) our analytical ISL approximation in §2.3. The result of their static approximation is that the larger minihalos ( $\geq \text{few} \times 10^5 - 10^6 M_{\odot}$ , depending on the red-

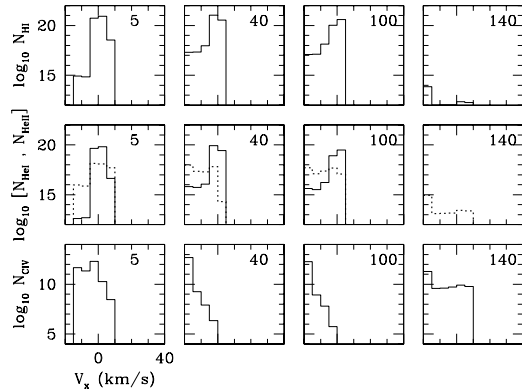


**Figure 32.** Same as Figure 31 but for BB 1e5 case.

shift and the source spectrum) were predicted not to evaporate completely but rather to leave a significant fraction of the gas (20%–40% for QSO-type power-law spectrum for  $10^7 M_\odot$  halo at  $z = 8 - 20$ ) still gravitationally bound to the minihalo. Our illustrative simulations demonstrate that when dynamical evolution is included this is not the correct outcome and all the gas is evaporated from the minihalos, leaving behind only a dark matter halo almost completely devoid of gas. In a companion paper, we will extend these studies to show that this conclusion holds for all minihalos, independent of their mass and redshift of collapse.

We have also shown here that a hydrodynamical treatment of the photoevaporation of minihalos which fails to include radiative transfer (i.e. the zero optical depth approximation) is also not adequate for describing this problem. Such an approximation yields a spherically-symmetric outflow and uniformly high ionization structure which differ greatly from the more realistic results reported here which take radiative transfer into account. As a consequence, any observable features, such as absorption lines, would not be predicted correctly by this approximation. The difference between more realistic simulations like ours, which include radiative transfer, and those which neglect optical depth can have profound consequences for the theory of cosmic reionization, as well.

Haiman, Abel & Madau (2001) pointed out the potential importance of minihalos as sinks of ionizing photons during reionization, due to the increased recombination rate inside these high-density regions. In §2.5, we described how these authors estimated, in the optically-thin limit, the number of ionizing photons per atom  $\xi = n_\gamma/n_a$  needed to evaporate a minihalo. They concluded from this that the clumping due to minihalos can easily raise the number of photons required to complete reionization by an order of magnitude or more compared to estimates that ignored the minihalos. This prompted them to identify a photon budget problem when comparing the requirements for reionizing the universe

with the available photon supply. In this paper, we have used our self-consistent gas dynamics and radiative transfer simulations to calculate  $\xi$  under more realistic assumptions. We have shown that the effect of ignoring radiative transfer and its feedback on the gas dynamics is to significantly overestimate  $\xi$ . For the illustrative cases shown here, we find that  $\xi$  was overestimated by a factor as large as 30–50, depending on the ionizing spectrum. In terms of the efficiency factor in equations (31) and (32), this means that we have found values of  $f \sim 1/30$  to  $1/50$ , depending on the spectrum of the ionizing sources. Optically-thin estimates also do not account for differences due to differences in the external source spectra. We have shown that photoevaporation by Pop. III stars is significantly more efficient in terms of the net photon consumption by this process than is photoevaporation by QSO or Pop. II stellar sources, even when all sources emit the same number of H ionizing photons per unit time. These effects may help alleviate the photon budget problem posed by Haiman, Abel & Madau (2001), especially if Pop. III sources dominated reionization.

Although we find here that  $\xi$  is smaller than previously estimated, the effects of minihalos as screens and of their evaporation as a sink of ionizing photons during reionization may still be considerable. For one, we find  $\xi \sim 5$ , which is still large compared to unity. In addition, this value applies only to the particular illustrative case of a  $10^7 M_\odot$  minihalo exposed to a source with flux  $F_0 = 1$  at  $z = 9$ . Only after we also calculate the values of  $\xi$  per minihalo for the full range of minihalo masses and redshifts and of source fluxes which can occur during reionization can we determine the full impact of the minihalos on that process. We will report those results in a companion paper to follow. However, we can already see that, if the reionization epoch was extended in time, as described in §1.2, with the final overlap of isolated H II regions occurring at  $z < 9$ , then the neutral regions which were ionized during this late phase had a significant fraction ( $\gtrsim 30\%$ ) of their baryons collapsed into minihalos. In that case, minihalo photoevaporation by the global I-fronts which reionized the universe is likely to have dominated this final “overlap” phase.

Apart from the destructive effects of intergalactic I-fronts on minihalo gas content described here, it has also been suggested that the same I-fronts might, instead, have a positive feedback effect on the minihalos rather than photoevaporating them entirely. It has been proposed, for example, that under certain conditions, external ionizing radiation can cause the implosion of the minihalo gas, leading to the formation of globular clusters (Cen 2001). We have not observed such an effect in our simulations.

Finally, we note that intervening minihalos are expected to be ubiquitous along the line of sight to high redshift sources (Shapiro 2001). With photoevaporation times  $t_{ev} \gtrsim 100$  Myr, this process can continue down to redshifts significantly below  $z = 10$ . For stellar sources in the  $\Lambda$ CDM model, our simulations show that photoevaporation of a  $10^7 M_\odot$  minihalo which begins at  $z_{initial} = 9$  can take 150 Myr to finish, at  $z_{final} = 7$ , during which time such minihalos

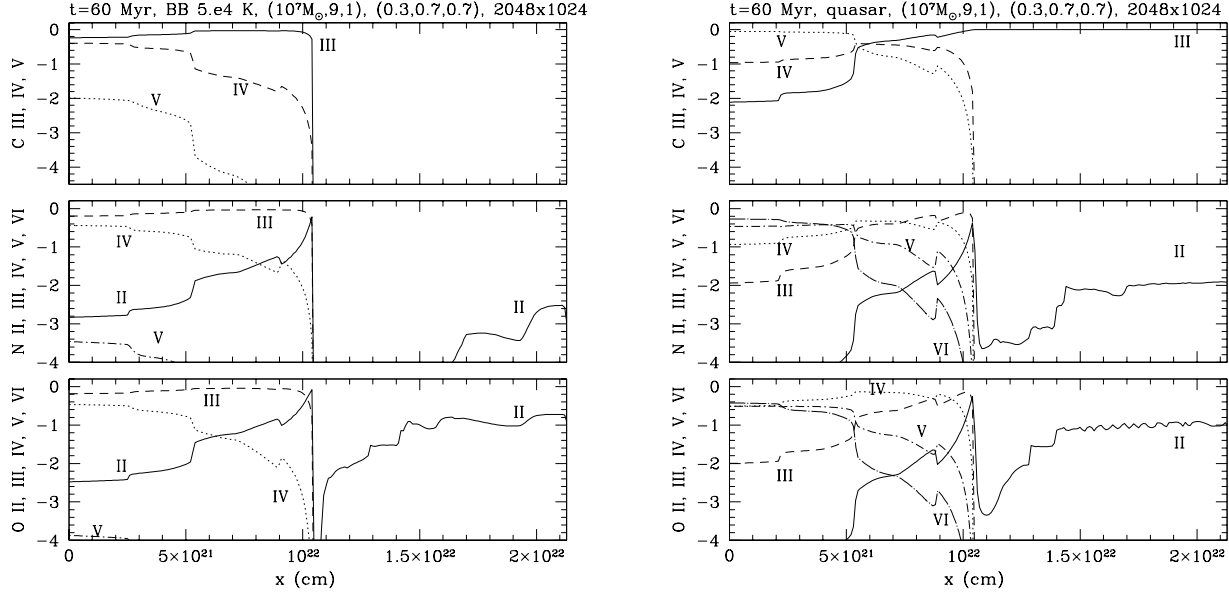


**Figure 33.** Observational diagnostics II: ionization structure of metals. C, N, and O ionic fractions along symmetry axis at  $t = 60$  Myr, for photoevaporating minihalo (a) (left) BB 5e4 case; (b) (right) QSO case.

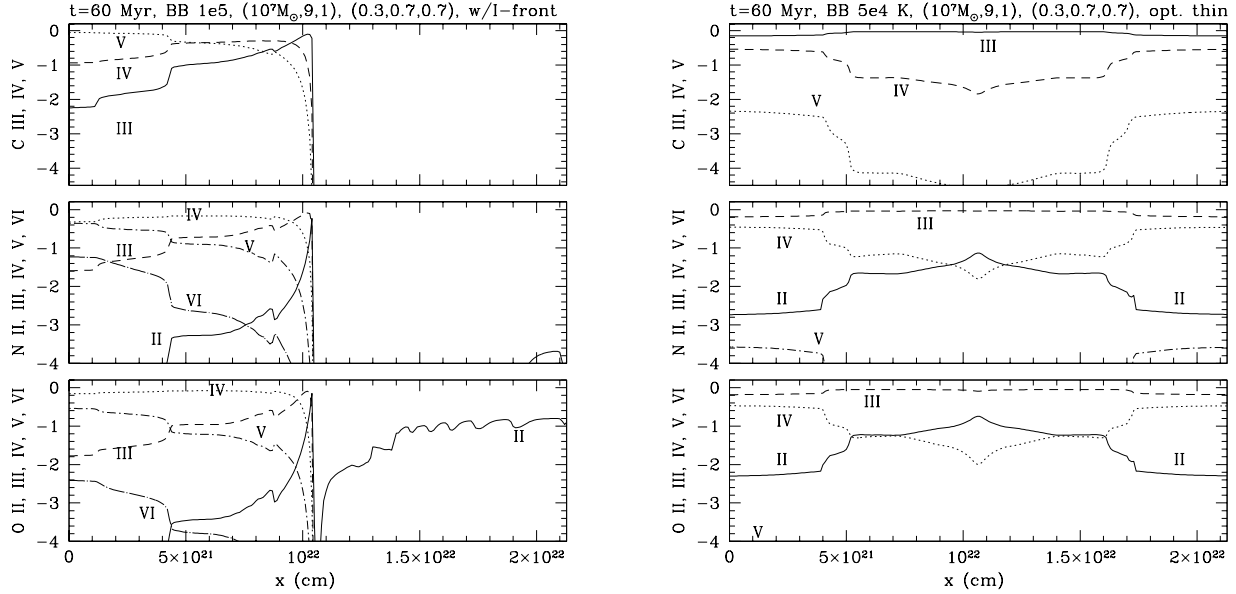


**Figure 34.** (a) (left) Same as Figure 33, but for BB 1e5 case. (b) (right) Same as Figure 33, but for optically-thin BB 5e4 case.

can survive without merging into larger halos. Observations of the absorption spectra of high redshift sources like those which reionized the universe should reveal the presence of these photoevaporative flows and provide a useful diagnostic of the reionization process.

## ACKNOWLEDGMENTS

We thank Garrelt Mellema for sharing his microphysics solver with us, for many useful discussions and for a careful reading of an early version of this manuscript. We thank

Hugo Martel for discussion and collaboration on various aspects of the role of minihalos which directly impacts the work reported here. We thank Marcelo Alvarez for his help in the visualization of our simulation results. This research was supported by NSF grant INT-0003682 from the International Research Fellowship Program and the Office of Multidisciplinary Activities of the Directorate for Mathematical and Physical Sciences, the Research and Training Network “The Physics of the Intergalactic Medium” set up by the European Community under the contract HPRN-CT2000-00126 RG29185 NASA ATP Grant NAG5-10825, and Texas Advanced Research Program Grant 3658-0624-1999.

## REFERENCES

- Abel T. Bryan G. L. & Norman M. L. 2002, *Science*, 295, 93
- Abel T. Norman M. L. & Madau P. 1999, *ApJ*, 523, 66
- Arthur S. J. 1991, PhD Thesis, University of Leeds
- Barkana R. & Loeb A. 1999, *ApJ*, 523, 54
- Barkana R. & Loeb A. 2002, *ApJ*, 578, 1
- Becker R. H. et al. 2001, *AJ*, 122, 2850
- Bertoldi F. 1989, *ApJ*, 346, 735
- Bertoldi F. & Draine B. 1995, *ApJ*, 458, 222
- Bertoldi F. & McKee C. F. 1990, *ApJ*, 354, 529
- Bertschinger E. 1985, *ApJS*, 58, 39
- Binney, J. and Tremaine, S. 1987 *Galactic Dynamics* Princeton: Princeton University Press
- Bond J. R., Szalay A. S. & Silk J. 1988, 324, 627
- Bromm V., Coppi P. S., & Larson R. B. 2002, *ApJ*, 264, 23
- Bromm V., Kudritzki R. P., & Loeb A. 2001, *ApJ*, 552, 464
- Cen R. 2001, *ApJ*, 560, 592
- Cen R. 2002, *ApJS*, 141, 211
- Cen R. & McDonald P. 2002, *ApJ*, 570, 457
- Ciardi B., Ferrara A., Marri S. & Raimondo G. 2001, *MNRAS*, 324, 381
- Ciardi B., Stoehr F., & White S. D. M. 2003, preprint (astro-ph/0301293)
- Djorgovski S. G., Castro S., Stern D., & Mahabal A. A. 2001, *ApJ*, 560, 5
- Fan, X. et al. 2000, *AJ*, 120, 1167
- Fan, X. et al. 2002, *AJ*, 123, 1247
- Fan, X. et al. 2003, *AJ*, 125, 1649
- Gnedin N. Y. 2000, *ApJ*, 535, 530
- Gnedin N. Y. & Abel T. 2001, *NewA*, 6, 437
- Gorti U. & Hollenbach D. 2001, *ApJ*, 573, 215
- Haiman Z., Abel T., & Madau P. 2001, *ApJ*, 551, 599
- Haiman Z., Abel T., & Rees M. J. 2000, *ApJ*, 534, 11
- Hayes J. C. & Norman M. L. 2002, preprint (astro-ph/0207260)
- Hui L. & Haiman Z. 2003, *ApJ*, preprint (astro-ph/0302439)
- Iliev I. T., & Shapiro P. R. 2001, *MNRAS*, 325, 468
- Iliev I. T. & Shapiro 2002, in *The Mass of Galaxies at Low and High Redshift*, eds. R. Bender and A. Renzini, ESO Astrophysics Symposia, Springer, p. 160 (astro-ph/0112427)
- Klein R. I., Sandford M. T. & Whitaker R. W. 1982, *ApJ*, 271, L69
- Kogut A. et al. 2003, *ApJ*, in press (astro-ph/0302213)
- Lefloch B. & Lazareff B. 1994, *A&A*, 289, 559
- Leitherer C. et al. 1999, *ApJS*, 123, 3
- Lizano S., Canto J., Garay G. & Hollenbach D. 1996, *ApJ*, 468, 739
- Madau P. & Rees M. J. 2000, *ApJ*, 542, L69
- Mellema G. 1993, PhD thesis, University of Leiden
- Mellema G., Raga A. C., Canto J., Lundquist P., Balick B., Steffen W., & Noriega-Crespo A. 1998, *A&A*, 331, 335
- Miralda-Escude J., Haehnelt M., & Rees M. J., 2000, *ApJ*, 530, 1
- Nakamoto T., Umemura M., & Susa H. 2001, *MNRAS*, 321, 593
- Oh, P., & Haiman, Z. 2003, preprint (astro-ph/0307135)
- Oort J. H. & Spitzer L. R. 1955, *ApJ*, 121, 6
- Raga A. C., Mellema G., & Lundquist P. 1997, *ApJS*, 109, 517
- Raga A. C., Taylor S. D., Cabrit S., & Biro S. 1995, *A&A*, 296, 833
- Razoumov A. O. & Scott D. 1999, *MNRAS*, 309, 287
- Ricotti M., Gnedin N. Y. & Shull J. M. 2002a, *ApJ*, 575, 33
- Ricotti M., Gnedin N. Y. & Shull J. M. 2002b, *ApJ*, 575, 49
- Sandford M. T., Whitaker R. W. & Klein R. I., 1983, *ApJ*, 271, L69
- Schmidt-Voigt M. & Koeppen J. 1987, *A&A*, 174, 211
- Shapiro P. R. 1986, *PASP*, 98, 1014
- Shapiro, P. R. 2001, in *Relativistic Astrophysics: 20th Texas Symposium*, eds. J. C. Wheeler and H. Martel (AIP Conference Proceedings Vol. 586), pp. 219-232
- Shapiro P. R. & Giroux M. L. 1987, *ApJ*, 321, L107
- Shapiro P. R., Iliev I. T., & Raga, A. C. 1999, *MNRAS*, 307, 203
- Shapiro P. R., Iliev I. T., Raga, A. C. & Martel H. 2003, in *The Emergence of Cosmic Structures, The 13th Annual October Astrophysics Conference in Maryland*, eds. S. Holt and C. Reynolds (AIP Conf. Series), pp. 89 (astro-ph/0302339)
- Shapiro P. R. & Kang H. 1987, *ApJ*, 318, 32
- Shapiro P. R. & Raga A. C. 2000, in *Astrophysical Plasmas: Codes, Models, and Observations*, eds. S. J. Arthur, N. Brickhouse, and J. J. Franco, *Rev.Mex.A.A. (SC)*, 9, 292
- Shapiro P. R. & Raga A. C. 2000, in *Cosmic Evolution and Galaxy Formation: Structure, Interactions, and Feedback* (ASP Conference Series, vol. 215), eds. J. Franco, E. Terlevich, O. Lopez-Cruz, and I. Aretxaga, pp. 1-6
- Shapiro P. R. & Raga A. C. 2001, in *The Seventh Texas-Mexico Conference on Astrophysics: Flows, Blows, and Glows*, eds. W. Lee and S. Torres-Peimbert, *Rev.Mex.A.A. (SC)*, vol. 10, pp. 109-114
- Shapiro P. R., Raga A. C. & Mellema G. 1997, in *Structure and Evolution of the Intergalactic Medium from QSO Absorption Line Systems* (Proceedings of the 13th IAP Astrophysics Colloquium), eds. P. Petitjean and S. Charlot,



- pp. 41–45  
 Shapiro P. R., Raga A. C. & Mellema G. 1998, *MmSAI*, 69, 463  
 Sokasian A. et al. 2001, *NewA*, 6, 359  
 Spergel, D. et al. 2003, preprint (astro-ph/0302209)  
 Spitzer L. R. 1978, *Diffuse Matter in Space*, Wiley  
 Tan J. C. & McKee C. F. 2001 in *Starburst Galaxies: Near and Far*, eds. L. Tacconi and D. Lutz. Heidelberg: Springer-Verlag, p. 188 (astro-ph/0012005)  
 Tenorio-Tagle G., Bodenheimer P., Noriega-Crespo A. 1983, in *Workshop on model nebulae*, ed. D. Pequignot, Observatoire de Paris, p. 178  
 Tumlinson J., & Shull J. M. 2000, *ApJ*, 528, L65  
 van Leer B. 1982, *Lect. Notes in Phys.*, 170, 507

## APPENDIX A: A TIME-DEPENDENT MODEL FOR VIRIALIZED HALOS WITH COSMOLOGICAL INFALL

The initial conditions for our simulations are given by the TIS profile for both the gas and the dark matter density for the virialized halo, with zero bulk velocity, as described by Iliev & Shapiro (2001), and a matching spherical, self-similar infall profile as described by Bertschinger (1985) for the density and infall velocity outside the halo, appropriately generalized to the case of a low-density background universe models (Iliev & Shapiro 2001, Appendix A). The match of the post-shock gas in this infall solution to the TIS is discussed in detail in § 7.2 of Shapiro, Iliev & Raga (1999). This match is made possible by the fact that the TIS radius  $r_t$  is almost coincident with the shock radius of the self-similar infall solution  $r_S$ , with the latter larger than the former by only 1.8%.<sup>4</sup> In order to match the two solutions seamlessly, we continue both the density and the velocity profiles of the infall solution down to  $r_t$ . For the velocity profile outside the TIS outer radius we use the pre-shock infall profile of the self-similar solution. Following the notation of Bertschinger (1985), we define the dimensionless radius  $\lambda \equiv r/r_{ta}(t)$ . Here  $r_{ta}$  is the turnaround radius of the shell which is just reaching maximum expansion at time  $t$ , whose time-dependence is given by  $r_{ta}(t) = r_{ta}(t_i)(t/t_i)^{8/9}$ , where  $t_i$  is our initial time. Due to self-similarity of the solution every feature in radius occurs at some fixed value of  $\lambda$ . For example, the location of the shock is given by  $\lambda_S = 0.338976$ , and the time-varying shock radius must follow  $r_S(t) = r_{ta}(t)\lambda_S$ . Similarly, the radial parameters of the TIS profile, like core radius  $r_0$  and  $r_t$ , follow the same time dependence with  $\lambda = (\lambda_0, \lambda_t) = (0.0113175, 0.3327339)$ , respectively.

The physical velocity  $v$  at a given radius  $r \geq r_t$  at a time  $t$  is given by the following parametric solution:

$$\lambda(\theta) = \sin^2 \frac{\theta}{2} \left( \frac{\theta - \sin \theta}{\pi} \right)^{-8/9} \quad (\text{A1})$$

and

$$v = \frac{r \sin \theta (\theta - \sin \theta)}{t (1 - \cos \theta)^2} = \frac{r_0(t)}{\lambda_0 t} V(\lambda), \quad (\text{A2})$$

where  $0 \leq \theta \leq 2\pi$ . For the TIS density profile we use the fitting formula to the exact numerical results given in Appendix B of Iliev & Shapiro (2001). The resulting initial condition for our simulations is shown in Figure 4.

In order to evolve the initial dark matter profile with time self-consistently, we assume that the mass of the TIS grows over time as a result of the infall, and our initial solution for the TIS gives way to a sequence of equilibrium TIS models, where the TIS is specified at each time by the mass  $M(t)$  and redshift  $z_{\text{coll}}$  at that time. Below we give the time-dependences of all relevant quantities.

The time-dependence of  $M(t)$  corresponds to that of the sphere bounded by the accretion shock in the Bertschinger solution. The central density  $\rho_0$  of our TIS solution is just proportional to the mean background density at the same epoch. At the early times of interest to us here, this dependence is simply  $\rho_0(t) = \rho_0(t_i)(t/t_i)^{-2}$ . With this scaling we can write the growth of the total mass with time as

$$\begin{aligned} M_{\text{TIS}}(t) &= M_{\text{TIS}}(t_i) \left[ \frac{r_{ta}^3(t)}{r_{ta}^3(t_i)} \right] \left[ \frac{\rho_b(t)}{\rho_b(t_i)} \right] \\ &= M_{\text{TIS}}(t_i) \left( \frac{t}{t_i} \right)^{2/3}. \end{aligned} \quad (\text{A3})$$

In fact, for any radius which grows in time self-similarly (i.e. keeping its  $\lambda$ -value constant) the mass interior to this radius must grow according to

$$m(\lambda, t) = m(\lambda, t_i) \left( \frac{t}{t_i} \right)^{2/3}. \quad (\text{A4})$$

The gravitational acceleration,  $g$ , at radius  $r$  of this assumed matter distribution is given simply in terms of the mass  $m(r)$  interior to this radius:  $g = Gm(r)/r^2$ . For fixed  $\lambda$ ,  $m(\lambda, t) \propto t^{2/3}$ , so we need only determine  $m(r, t) = m[\lambda(r, t), t]$  at fixed  $r$  for different times. This is given by

$$m(\lambda, t) = M(\lambda) \frac{4\pi\rho_b(t_i)r_S^3}{3\lambda_S^3} \left( \frac{t}{t_i} \right)^{2/3}, \quad (\text{A5})$$

where

$$\lambda(r, t) = \frac{\lambda_0}{r_0(t_i)} \left( \frac{t}{t_i} \right)^{-8/9} r. \quad (\text{A6})$$

(A) For  $\lambda \geq \lambda_t = 0.332734$ , the infall mass profile is

$$M(\lambda) = -\frac{9}{2}\lambda^2 D(\lambda) \left[ V(\lambda) - \frac{8}{9}\lambda \right], \quad (\text{A7})$$

where  $V(\lambda)$  was defined in equation (A2) above and

$$D(\lambda) = \frac{9(\theta - \sin \theta)^2}{16 \sin^6(\theta/2) \{1 + 3[1 - 3V(\lambda)/(2\lambda)]\}} \quad (\text{A8})$$

(Bertschinger 1985).

<sup>4</sup> In this Appendix, spherical symmetry applies throughout, so we use the variable “ $r$ ” to mean the spherical radius here.

(B) For  $\lambda \leq \lambda_t$  the TIS mass profile is derived by enforcing hydrostatic equilibrium inside the TIS, using the density profile fitting formula and the isothermal virial temperature to solve for the gravitational acceleration needed to balance the pressure force:

$$M(\lambda) = 6\lambda_0 \left( \frac{\rho_0}{\rho_b} \right) \lambda^2 \times \frac{\xi [A/(a^2 + \xi^2)^2 - B/(b^2 + \xi^2)^2]}{[A/(a^2 + \xi^2) - B/(b^2 + \xi^2)]}, \quad (\text{A9})$$

where  $(A, a^2, B, b^2) = (21.38, 9.08, 19.81, 14.62)$ ,  $\xi = r/r_0$ ,  $r_0$  is the TIS core radius, and  $\rho_b$  is the mean background density.